

## CORONAVIRUS

# A lethal mouse model for evaluating vaccine-associated enhanced respiratory disease during SARS-CoV-2 infection

Naoko Iwata-Yoshikawa<sup>1†</sup>, Nozomi Shiwa<sup>1†</sup>, Tsuyoshi Sekizuka<sup>2</sup>, Kaori Sano<sup>1‡</sup>, Akira Ainal<sup>1</sup>, Takuya Hemmi<sup>1,3</sup>, Michiyo Kataoka<sup>1</sup>, Makoto Kuroda<sup>2</sup>, Hideki Hasegawa<sup>4</sup>, Tadaki Suzuki<sup>1</sup>, Noriyo Nagata<sup>1\*</sup>

One safety concern during severe acute respiratory syndrome coronavirus 2 (SARS-CoV-2) vaccine development has been the vaccine-associated enhanced disease, which is characterized by eosinophilic immunopathology and T helper cell type 2 ( $T_{H}2$ )-biased immune responses with insufficient neutralizing antibodies. In this study, we established a lethal animal model using BALB/c mice and a mouse-passaged isolate (QHmusX) from a European lineage of SARS-CoV-2. The QHmusX strain induced acute respiratory illness, associated with diffuse alveolar damage and pulmonary edema, in  $T_{H}2$ -prone adult BALB/c mice, but not in young mice or  $T_{H}1$ -prone C57BL/6 mice. We also showed that immunization of adult BALB/c mice with recombinant spike protein without appropriate adjuvant caused eosinophilic immunopathology with  $T_{H}2$ -shifted immune response and insufficient neutralizing antibodies after QHmusX infection. This lethal mouse model is useful for evaluating vaccine-associated enhanced respiratory disease during SARS-CoV-2 infection and may provide new insights into the disease pathogenesis of SARS-CoV-2.

Copyright © 2022  
The Authors, some  
rights reserved;  
exclusive licensee  
American Association  
for the Advancement  
of Science. No claim to  
original U.S. Government  
Works. Distributed  
under a Creative  
Commons Attribution  
NonCommercial  
License 4.0 (CC BY-NC).

## INTRODUCTION

Since the end of 2019, a novel coronavirus, severe acute respiratory syndrome coronavirus 2 (SARS-CoV-2), which causes coronavirus disease 2019 (COVID-19), rapidly spread from Wuhan, China to the rest of the world, threatening lives and society on a global level (1–3). On 30 January 2020, the World Health Organization declared the COVID-19 outbreak as a public health emergency of international concern and reached consensus on the need to accelerate research to stop the outbreak by developing easy-to-apply diagnoses, accelerating existing vaccine candidates, and preventing infection (4). Since then, more than 50 clinical trials are ongoing, and few of the vaccine candidates have been approved. It is necessary to ensure the safety of these vaccines; however, there are some concerns regarding coronavirus vaccine development (5).

Previous studies have shown that an inactivated SARS-CoV vaccine induces neutralizing antibodies in mouse models; however, the immunized mice showed eosinophilic immunopathology of the lungs upon SARS-CoV challenge (6, 7). This is thought to be due to the production of insufficient amounts of antibodies against SARS-CoV and a skewed immune response toward T helper cell type 2 ( $T_{H}2$ ) (6, 7), which are thought to be caused by nucleocapsid (N)-specific immune responses and enhanced eosinophilic immunopathology resulting from the incorporation of SARS-CoV N into vaccine formulations (7–9). The SARS-CoV spike (S) protein vaccine also induced a similar eosinophilic immunopathology in a mouse model (10).

Vaccine-induced eosinophilic immunopathology in murine lungs upon viral infection was reduced by Toll-like receptor (TLR) agonist adjuvants (11).

A similar lung pathology has been reported for vaccine-associated enhanced respiratory disease, which was recognized in the 1960s with the advent of formalin-inactivated respiratory syncytial virus (FI-RSV) and measles vaccines (12). During clinical trials for the RSV vaccine candidate, 80% of vaccine-immunized children were hospitalized, and two children died of enhanced respiratory disease upon subsequent RSV infection (13). Histological examination revealed that bronchoconstriction and severe pneumonia with unexpected peribronchiolar eosinophilic infiltration occurred in the children's lungs (14, 15). Immune complex formation and complement activation were detected in small airways using postmortem lung sections from fatal cases with enhanced RSV disease (15). Further studies on the FI-RSV vaccine reproduced similar disease enhancement in BALB/c mice and also suggested that a skewed  $T_{H}2$  immune response and an insufficient neutralizing antibody response caused eosinophilic immunopathology in the lungs (16–18). The generation of nonprotective antibodies by the FI-RSV vaccine was due to poor TLR stimulation (18). Because similar eosinophilic immunopathology was observed in mouse models for SARS-CoV and also for Middle East respiratory syndrome (MERS)-CoV vaccine studies (6–9, 11, 19–21), there are also concerns regarding the possibility of vaccine-associated enhanced respiratory disease in humans immunized with SARS-CoV-2 candidate vaccines.

Because the features of clinical illness associated with SARS-CoV-2 infection in Syrian hamsters are very clear, this small animal model is considered useful for screening therapeutics and evaluating the efficacy of candidate vaccines (22). However, vaccine-associated enhanced respiratory disease was not observed in the lungs or livers of hamsters following SARS-CoV infection (23), and it has not yet been observed in SARS-CoV-2 studies. SARS-CoV-2 has very low affinity for the murine angiotensin-converting enzyme 2 (ACE2)

<sup>1</sup>Department of Pathology, National Institute of Infectious Diseases, 208-0011 Tokyo, Japan. <sup>2</sup>Pathogen Genomics Center, National Institute of Infectious Diseases, 162-8640 Tokyo, Japan. <sup>3</sup>Department of Biological Science and Technology, Tokyo University of Science, 125-8585 Tokyo, Japan. <sup>4</sup>Influenza Virus Research Center, National Institute of Infectious Diseases, 208-0011 Tokyo, Japan.

\*Corresponding author. Email: nnagata@nih.go.jp

†These authors contributed equally to this work.

‡Present address: Department of Microbiology, Icahn School of Medicine at Mount Sinai, New York, NY, USA.

receptor; thus, this virus does not easily infect wild-type laboratory mice. To establish a murine model for COVID-19, transgenic mice bearing the human ACE2 receptor, which were already established after the SARS-CoV outbreak in 2003, were studied (24), and mouse-adapted SARS-CoV-2 was rapidly produced using reverse genetics methodology (25). On the other hand, Gu *et al.* (26) successfully adapted a clinical isolate of SARS-CoV-2 by serial passaging in the respiratory tract of aged BALB/c mice. Considering its convenience, we also set out to produce a mouse-passaged virus using an isolate similar to the one in a previous SARS-CoV study (27). Fortunately, we obtained a SARS-CoV-2 isolate of European lineage (D614G) that could be serially passaged in young BALB/c mice *in vivo*. This strain, passaged 10 times in mice, was highly infective in inbred mice, such as BALB/c and C57BL/6; in addition, adult BALB/c mice became moribund after experimental infection. In this study, we produced a lethal BALB/c mouse model for evaluating vaccine efficacy and vaccine-associated enhanced respiratory disease upon infection with mouse-passaged SARS-CoV-2.

## RESULTS

### Serial *in vivo* passaging of SARS-CoV-2 in young BALB/c mice

One isolate of the Wuhan lineage (2019-nCoV/Japan/TY/WK-521/2020), referred to as the WK-521 strain, and one isolate of the European lineage (hCoV-19/Japan/QH-329-037/2020), referred to as the QH-329-037 strain, were used to evaluate infectivity in immunocompetent, inbred, 4-week-old BALB/c mice ( $n = 4$ ) (Table 1). Both animals challenged with QH-329-037 or WK-521 showed no clinical symptoms or obvious weight loss up to 3 days postinoculation (p.i.); however, the infectious virus was recovered from the respiratory tract of QH-329-037-inoculated mice with titers of around  $10^3$ – $50\%$

tissue culture infectious dose/ml (TCID<sub>50</sub>/ml) in the lung lavage and lung homogenates (fig. S1, A and B). Then, the lung lavage sample from the QH-329-037 group was serially passaged in young BALB/c mice (4- to 6-week-old females,  $n = 3$  to 4) by intranasal inoculation. During 10 serial passages [referred to as P1 to P10 in fig. S1 (C and D)] of the QH-329-037 strain of SARS-CoV-2, the virus was consistently identified in the lung lavage by quantitative polymerase chain reaction (PCR) (fig. S1C) and viral titration in transmembrane protease serine type 2-expressing (TMPRSS2)-VeroE6 cells (fig. S1D). After 10 serial passages *in vivo*, the lung lavage sample was propagated in VeroE6/TMPRSS2 cells twice [referred to as P1d1 and P2d1 in fig. S1 (C and D)] and then stored at  $-80^\circ\text{C}$  as stock and working viral solutions, respectively (referred to as QHmusX). Overall, the SARS-CoV-2 isolate of the European lineage, QH-329-037, was successfully passaged serially *in vivo* using young BALB/c mice.

### Experimental infection of BALB/c mice with mouse-passaged SARS-CoV-2

Advanced age is associated with higher mortality rates in COVID-19 cases (28). In previous SARS-CoV studies, young and adult BALB/c mice showed different outcomes after intranasal infection with mouse-passaged strains, analogous to SARS cases in humans (27, 29). Thus, we used 4-week-old and 6-month-old female BALB/c mice for experimental infection with SARS-CoV-2 (Fig. 1A). Dulbecco's modified Eagle's medium (DMEM) was used for mock infections. After intranasal inoculation with the original QH-329-037 isolate and the mouse-passaged QHmusX strain ( $2.3 \times 10^5$  TCID<sub>50</sub> per mouse; 30  $\mu\text{l}$ ), none of the mice inoculated with QH-329-037 showed any symptoms including weight loss, while mice inoculated with QHmusX lost weight within 2 days p.i. Four-week-old BALB/c mice inoculated with QHmusX showed transient weight loss within

**Table 1. SARS-CoV-2 strains in this study.** Anti-mycoplasma reagents (MC-210; 0.5  $\mu\text{g}/\text{ml}$ ; Waken, Kyoto, Japan) were used to eradicate *Mycoplasma* from the cells and virus stock during virus propagation from passages 4 to 6. The passage 7 virus stock was assessed, and the genome sequences were deposited in the DNA Data Bank of Japan. A single-nucleotide polymorphism with a synonymous mutation [Y7869 (cytosine: 90%, thymine: 10%)] in the open reading frame 1a (ORF1a) region was detected in the virus stock; this mutation was not present in the original WK-521 isolate. GISAID, Global Initiative on Sharing All Influenza Data.

Strain	Origin		Accession no. of original isolate	GISAID clade*/region of exposure (Pango lineage)	Passage history for the animal experiment in this study		Mycoplasma contamination in inoculum†
	Date collected	Specimen			Cell	Propagation (accession no.)	
2019-nCoV/ Japan/TY/WK521/2020	31 January 2020	Throat swab, returnee from Wuhan	EPI_ISL_408667	S/East Asia (lineage A)	VeroE6/TMPRSS2	9 passages‡ (SAMD00320668)	Negative
hCoV-19/ Japan/QH-329-037/2020	29 March 2020	Throat swab returnee from European Union	EPI_ISL_529135	G/Europe (lineage B.1)	VeroE6/TMPRSS2	4 passages	Positive
QHmusX	12 August 2020	Lung lavage from 10 times passaged QH-329-037 in BALB/c mice	LC605054	–	VeroE6/TMPRSS2	2 passages, following 10 passages in mice	Negative

\*GISAID clades were obtained from "Clade and lineage nomenclature, July 4, 2020" ([www.gisaid.org/references/statements-clarifications/clade-and-lineage-nomenclature-aids-in-genomic-epidemiology-of-active-hcov-19-viruses/](http://www.gisaid.org/references/statements-clarifications/clade-and-lineage-nomenclature-aids-in-genomic-epidemiology-of-active-hcov-19-viruses/)). †Mycoplasma contamination was detected by PCR (TaKaRa PCR Mycoplasma Detection Set, TaKaRa, Shiga, Japan). ‡WK-521 was isolated from VeroE6/TMPRSS2 cells contaminated with *Mycoplasma hyorhinis* and *Mycoplasma arginini* (47).

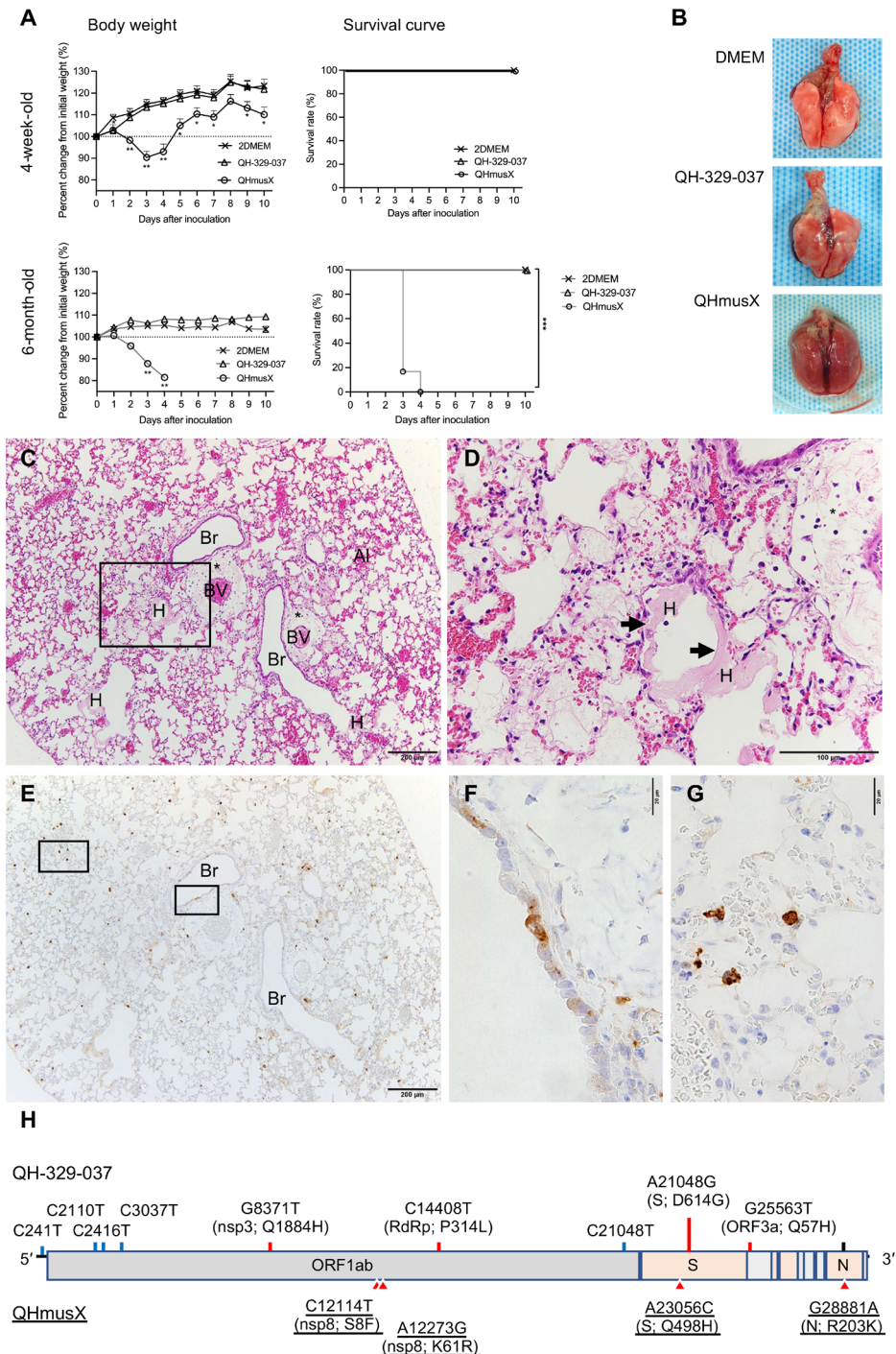


**Fig. 1. Experimental infection of BALB/c mice with SARS-CoV-2.** Female BALB/c mice (4 weeks old and 6 months old) were inoculated with QH-329-037 or QHmusX. Control mice were inoculated with cell culture medium (DMEM). (A) Curves depicting body weight and survival for 10 days p.i. ( $n=6$ ). Error bars represent SEs. For body weight curves,  $*P<0.05$  and  $**P<0.01$  by Mann-Whitney test; for survival curves,  $***P<0.001$  by log-rank (Mantel-Cox) test. (B) Gross lung pathology at the end point of mice inoculated with SARS-CoV-2. Photo credit: Noriyo Nagata, National Institute of Infectious Diseases. (C) Histopathological findings in the lungs of a moribund adult mouse at 3 days p.i. Br, bronchiole; Al, alveoli; BV, blood vessel; H, hyaline membrane. \*, perivascular edema. (D) A higher-magnification image of the boxed area in (C). (E) Immunohistochemical staining using anti-SARS-CoV-2 N-specific antibody. (F and G) Higher-magnification images of the boxed area in (E). (H) Diagram of the SARS-CoV-2 genome. QH-329-037 has nine mutations compared with the Wuhan-Hu-1 strain shown in the upper part of the genome diagram. Blue bars, synonymous mutations; red bars, nonsynonymous mutations. A single-nucleotide polymorphism is present at position 28,881 (G:A = 53.26:46.74), which results in an amino acid change in the N gene (N; R203K) (black bar). Lower highlight (red triangles) shows the sites of differences between the original isolate QH-329-037 and QHmusX. QHmusX has four mutations compared with the QH-329-037 strain. Position numbers are relative to those in the reference Wuhan sequence (MN908947.3). nsp, nonstructural protein; RdRp, RNA-dependent RNA polymerase; ORF, open reading frame.

3 days p.i. and recovered without respiratory illness; however, all 6-month-old BALB/c mice inoculated with QHmusX showed clinical illness, such as ruffled fur and low activity levels within 2 days p.i., and then developed severe acute respiratory illness with significant weight loss (Fig. 1A). Overall, when infected with QHmusX, all 4-week-old mice survived, but 6-month-old mice became moribund within 4 days p.i. Moribund 6-month-old mice showed massive pulmonary edema in whole lung lobes grossly (Fig. 1B). Histopathological examination revealed that diffuse alveolar damage was associated with viral infection and severe illness (Fig. 1C). Hyaline membrane formation was seen in several alveoli with massive edema and very slight inflammatory infiltration (Fig. 1D). Many viral antigen-positive cells were found in the bronchi, the bronchioles, and the alveolar area in all lung lobes (Fig. 1, E to G). Viral replication was also observed in the nasal cavity, which was accompanied by slight inflammatory reactions on day 3 p.i. (fig. S2). Other organs, including the brain, heart, liver, spleen, intestine, and kidneys, showed no lesions associated with viral replication by histopathology or immunohistochemistry. Thus, the SARS-CoV-2 QHmusX strain, passaged 10 times in mice, infected upper and lower respiratory tracts and induced lethal respiratory illness in adult BALB/c mice, but not in young BALB/c mice.

### Effect of the Q498H mutation on binding affinity for ACE2

Next, we confirmed variants of SARS-CoV-2 during in vivo passages by next-generation sequencing (NGS) analysis. NGS revealed that the viral genome isolated during in vivo passages using BALB/c mice harbored 12 single-nucleotide substitutions, including 6 nonsynonymous mutations in the open reading frame 1ab (ORF1ab) region, 2 nonsynonymous mutations in the S region, and 2 nonsynonymous mutations in each of the ORF3a and N regions (Table 2). The nonsynonymous mutation, Q498H in the S region related to receptor binding, appeared during the first passage in BALB/c mice. After three passages in vivo, all variants had the amino acid substitution (Q498H) that was maintained until the 10th passage and even after two propagations in VeroE6/TMPRSS2 cells. Viral propagation using VeroE6/TMPRSS2 cells caused two nonsynonymous mutations in the ORF1ab region. The consensus virus sequence of the mouse-passaged SARS-CoV-2, QHmusX, with two nonsynonymous mutations in the ORF1ab region, a nonsynonymous mutation in the S region, and a nonsynonymous mutation in the N region from the original isolate of QH-329-037 was used for animal experiments in this study (Fig. 1H).

To evaluate the impact of Q498H substitution on SARS-CoV-2 binding to human or murine ACE2, we produced SARS-CoV-2 trimeric S proteins using a mammalian cell protein expression system (fig. S3A) and conducted biolayer interferometry assays (fig. S3B). In addition to those of wild-type and Q498H S proteins, the affinities of recombinant S proteins with mutations harbored by other mouse-adapted SARS-CoV-2 viral strains to ACE2 were also evaluated. The Q498Y + P499T (25) and N501Y (26) mutations resulted in nonlethal virulence in BALB/c mice, while the combined Q493K + Q498Y + P499T mutation resulted in lethal infection in adult BALB/c mice (30). Wild-type S protein had strong affinity for human ACE2, whereas the Q498H, Q493K + Q498Y + P499T, and N501Y mutations caused an evident drop in affinity for human ACE2, with increased dissociation efficiency (fig. S3B). The Q498Y + P499T mutation did not alter the dissociation efficiency with human ACE2. By contrast, the wild-type S protein had low binding affinity

for murine ACE2, while S proteins with the mutations Q498H, Q493K + Q498Y + P499T, and N501Y had higher binding affinity than the wild-type S protein. Notably, the Q498H and Q493K + Q498Y + P499T mutations, harbored by lethal mouse-adapted viral strains, caused an evident increase in binding affinity compared with the other mutations harbored by nonlethal mouse-adapted viral strains. Notably, the single Q498H mutation caused both an increase in association efficiency and a decrease in dissociation efficiency, leading to an overall increase in binding affinity with murine ACE2. Thus, the mouse-passaged SARS-CoV-2 strain, QHmusX, acquired the S mutation Q498H during in vivo passages, which resulted in higher binding affinity for murine ACE2.

### Age- and strain-related differences in the pathophysiology of mice infected with mouse-passaged SARS-CoV-2

To establish a lethal respiratory mouse infection model with SARS-CoV-2, we determined the 50% lethal dose ( $LD_{50}$ ) for the QHmusX strain in 24-week-old BALB/c mice. Animals received intranasal inoculations (30  $\mu$ l) of  $2.3 \times 10^1$  to  $2.3 \times 10^5$  TCID<sub>50</sub> or DMEM ( $n = 7$  per group). The LD<sub>50</sub> [including the humane end point (respiratory distress, moribund, and more than 25% weight loss)] was  $4.4 \times 10^2$  TCID<sub>50</sub>/30  $\mu$ l in 24-week-old BALB/c mice, as determined by the Behrens-Kärber method (fig. S4, A and B).

Next, we evaluated the effect of age on the survival of mice after infection. BALB/c mice of various ages, including 4, 11, 17, and 24 weeks, were inoculated with  $2.3 \times 10^4$  TCID<sub>50</sub> of QHmusX ( $52LD_{50}$ ; more than  $10LD_{100}$  in 24-week-old BALB/c mice). All 11-week-old BALB/c mice showed ruffled hair, loss of appetite, and transient weight loss but recovered within 5 days p.i. By contrast, all 17-week-old BALB/c mice became moribund after inoculation with QHmusX (Fig. 2, A and B).

We then examined viral replication kinetics in the lungs of BALB/c mice at 6 hours p.i. and on days 1 to 4 p.i. ( $n = 4$ ). The viral titers in the lungs of each aged BALB/c mouse were between  $10^8$  and  $10^{10}$  TCID<sub>50</sub>/g at 1 day p.i.; these values were obviously higher than those at 6 hours p.i. Higher viral titers were detected in the lungs of 11-, 17-, and 24-week-old BALB/c mice from days 1 to 4 p.i. than those in 4-week-old BALB/c mice (Fig. 2C). There was no significant difference between the 11-week-old (nonlethal) and 17-week-old (lethal) groups. On days 3 and 4 p.i., significantly higher titers were observed in the 24-week-old group than in the other groups.

Next, we conducted more detailed immunopathological investigations to determine which host factors were related to infection outcome (Fig. 2D). Lower levels of granulocyte-macrophage colony-stimulating factor (GM-CSF) and higher levels of monocyte chemoattractant protein 1 (MCP-1) were observed in the lungs of 11-, 17-, and 24-week-old BALB/c mice than those in 4-week-old BALB/c mice. Lower levels of regulated upon activation, normal T cell expressed and secreted (RANTES), monokine induced by interferon- $\gamma$  (IFN- $\gamma$ ) (MIG), and IFN- $\gamma$  at days 3 and 4 p.i. were observed in the lungs of 17- and 24-week-old BALB/c mice (lethal) than those in 4- or 11-week-old mice (nonlethal). At 4 days p.i., predominantly high levels of interleukin-6 (IL-6) were detected in the lungs of 17- and 24-week-old BALB/c mice. In 24-week-old BALB/c mice, which showed aggressive clinical symptoms after infection, early expression of proinflammatory chemokines and cytokines, including macrophage inflammatory protein 1 $\alpha$  (MIP-1 $\alpha$ ), MIG, IL-12 (p40), IL-1 $\alpha$ , IL-1 $\beta$ , and tumor necrosis factor- $\alpha$  (TNF- $\alpha$ ), was observed in the lungs at 1 day p.i. These observations indicate that both viral

**Table 2.** SARS-CoV-2 variants during passages in BALB/c mice and after propagation in VeroE6/TMPRSS2 cells.

Nucleotide position MN908947.3	Gene (region)	Sequence variants*	Ratio of variant allele (%)										Propagated in VeroE6/TMPRSS2 cells		
			Original			Passaged in mice									
			QH-329-037	P1	P2	P3	P4	P5	P6	P7	P8	P9	P10	P1d1†	P2d1†
11,982	ORF1ab (nsp7)	c.11717A>C (p.Glu3906Ala)	0	58.12	0	0	0	0	0	0	0	0	0	0	0
12,114	ORF1ab (nsp8)	c.11849C>T (p.Ser3950Phe)	0	0	0	0	0	0	37.25	88.49	98.29	99.27	99.34	99.13	98.78
12,273	ORF1ab (nsp8)	c.12008A>G (p.Lys4003Arg)	0	0	92.61	100	99.96	99.85	99.91	99.92	99.82	99.95	99.88	99.84	99.92
12,357	ORF1ab (nsp8)	c.12092C>T (p.Thr403Ile)	0	0	0	0	0	0	0	0	0	0	0	0	28.8
13,197	ORF1ab (nsp10)	c.12932C>T (p.Thr431Ile)	0	0	0	0	0	0	0	0	0	0	0	0	21.85
19,648	ORF1ab (nsp15)	c.19333G>A (p.Val6462Ile)	0	0	0	20	27.98	0	0	0	0	0	0	0	26.46
20,841	ORF1ab (nsp16)	c.20576A>G (p.Val859Val)	0	61.97	0	0	0	0	0	0	0	0	0	0	0
23,039	S (S1 RBD) (p.Gln493Lys)	c.1477C>A (p.Gln493Lys)	0	51.98	0	0	0	0	0	0	0	0	0	0	0
23,056	S (S1 RBD) (p.Gln493His)	c.1494A>C (p.Arg493His)	0	30.08	93.63	100	99.95	99.92	99.88	99.81	100	99.87	99.9	99.93	99.92
25,418	ORF3a	c.26C>T (p.Thr9Ile)	0	0	70.78	41.7	49.11	41.54	30.55	0	0	0	0	0	0
26,442	E	c.198 T>C (p. Asn66Asn)	0	53.36	0	0	0	0	0	0	0	0	0	0	0
28,881	N	c.608G>A (p.Arg203Lys)	46.74	42.62	91.51	99.61	99.9	99.86	100	99.79	100	99.93	99.92	99.87	99.84

\*c. " represents a coding DNA sequence, and p. " represents a protein sequence.

†P1d1 and P2d1, viral stocks were harvested from the first (P1d1) and second (P2d1) propagations in VeroE6/TMPRSS2 cells at 1 day p.i.

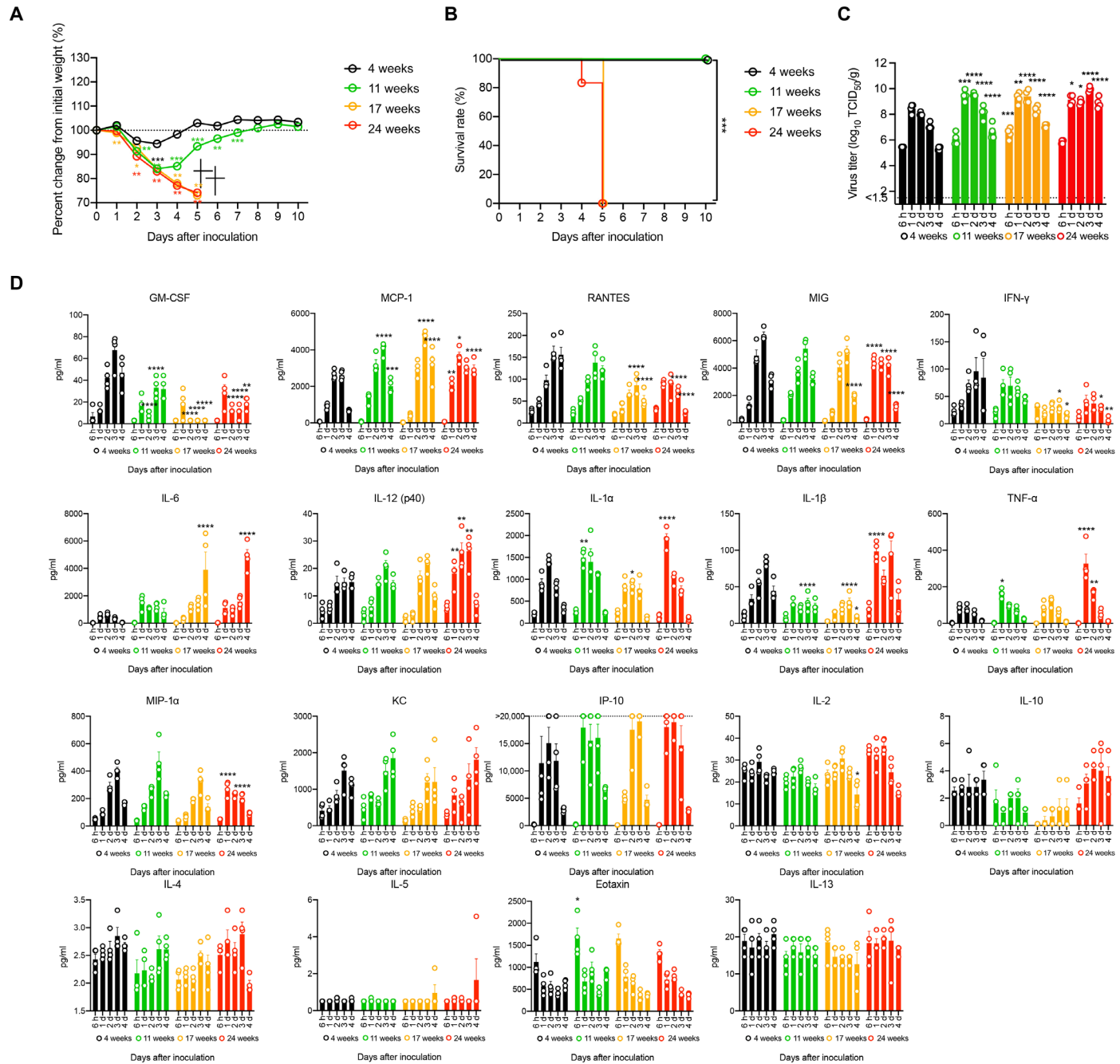


**Fig. 2. Age-dependent pathophysiology in BALB/c mice induced by mouse-passaged SARS-CoV-2.** Female BALB/c mice were inoculated intranasally with  $2.3 \times 10^4$  TCID<sub>50</sub> of QHMusX (52LD<sub>50</sub>; more than 10LD<sub>100</sub> in 24-week-old BALB/c mice). **(A)** Body weight curve of BALB/c mice inoculated with QHMusX. Asterisks indicate statistically significant differences between 4- and 11-, 17-, or 24-week-old BALB/c mice ( $n = 6$ ; \* $P < 0.05$ , \*\* $P < 0.01$ , and \*\*\* $P < 0.001$  by Mann-Whitney test). **(B)** Survival curve of animals from the same experiment as in (A) [ $n = 6$ ; \*\*\* $P < 0.001$  by log-rank (Mantel-Cox) test, compared with 4-week-old mice]. **(C)** Viral titers in lung homogenates at 6 hours and 1 to 4 days p.i. ( $n = 4$  per group). The detection limit was  $10^{1.5}$  TCID<sub>50</sub>/g of tissue. **(D)** Cytokine and chemokine levels in the lungs of BALB/c mice at different time points after inoculation ( $n = 4$  per group). Samples were from the same experiment as those in (C). Asterisks in (C) and (D) indicate statistically significant higher or lower levels in 11-, 17-, or 24-week-old BALB/c mice than in 4-week-old BALB/c mice. (C) and (D): \* $P < 0.05$ , \*\* $P < 0.01$ , \*\*\* $P < 0.001$ , and \*\*\*\* $P < 0.0001$  by Tukey's multiple comparison test.

replication and patterns of cytokine and chemokine responses are related to the different outcomes of the mice in the different age groups after OHmusX infection.

The lungs of infected 4- and 24-week-old animals were also used for sequential histopathological analyses on days 1 and 3 and at the

humane end point ( $n = 3$ ). On day 1, a very slight degeneration (i.e., vacuolar degeneration) was observed in the bronchiolar epithelium, whereas many viral antigen-positive cells were detected in the bronchioles from both groups (Fig. 3A). Ionized calcium-binding adapter protein 1 ( $\text{Iba-1}$ )<sup>+</sup>-activated macrophages and CD3<sup>+</sup>

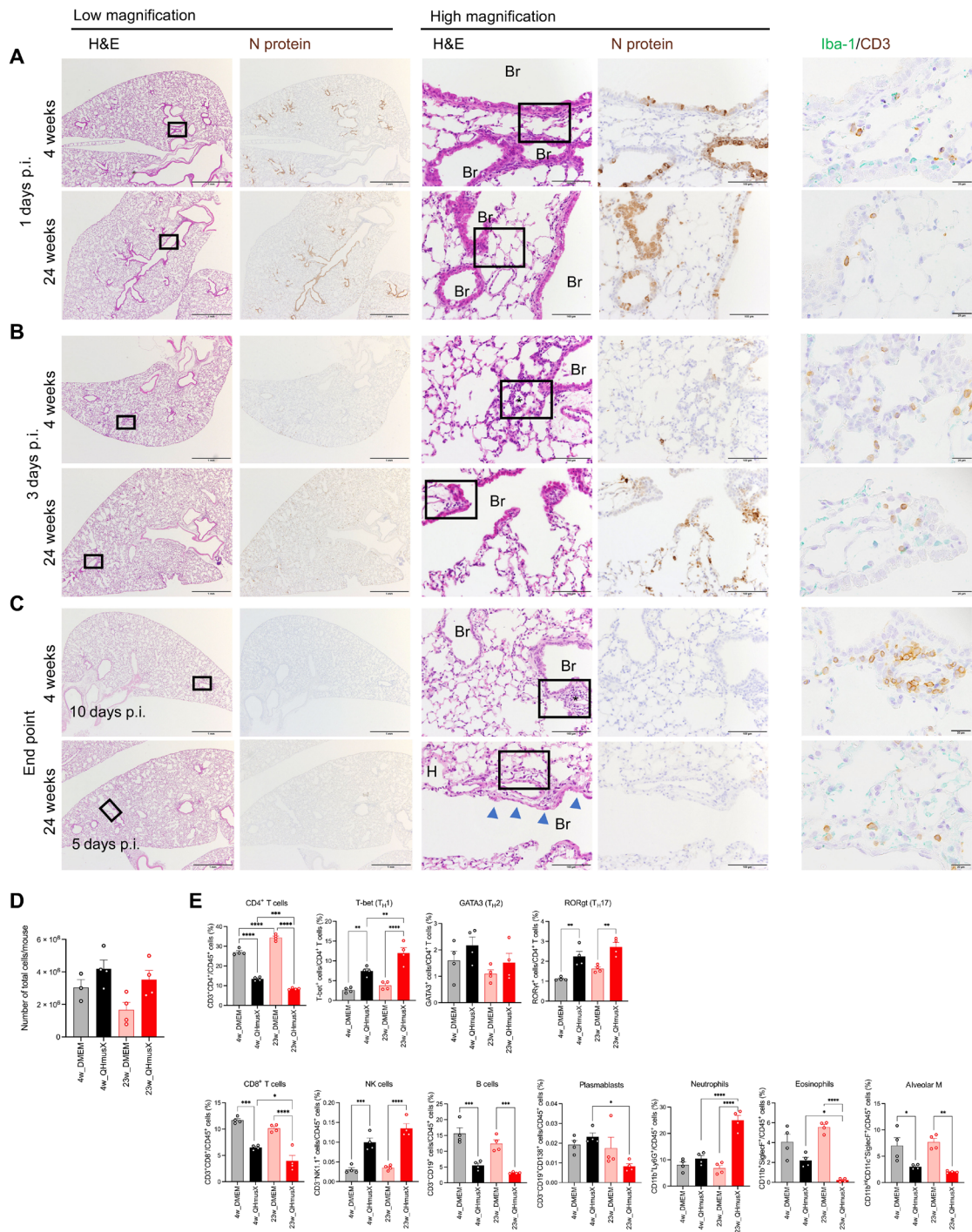


**Fig. 3. Age-dependent histopathological differences in BALB/c mice after infection with mouse-passaged SARS-CoV-2.** Female BALB/c mice were inoculated intranasally with  $2.3 \times 10^4$  TCID<sub>50</sub> QHmusX (52LD<sub>50</sub>, more than 10LD<sub>100</sub> in 24-week-old BALB/c mice). (A to C) Histopathological findings in the lungs of 4-week-old [top panels in (A) to (C)] and 24-week-old [bottom panels in (A) to (C)] mice on day 1 (A), day 3 (B), and at the end point (C). The results in each panel are representative of at least three mice for each panel. Immunohistochemical staining with anti-SARS-CoV-2 N-specific antibody (SARS-CoV-2) revealed viral antigen-positive cells (brown) in pulmonary epithelial cells of the bronchioles and alveolar area. Higher-magnification images are the boxed area in the low-magnification panels. Scale bars, 1 mm for low magnification and 100  $\mu$ m for high magnification. Right (Iba-1/CD3): Inflammatory cells in the lesion by double immunohistochemical staining for Iba-1 (green) and CD3 (brown) markers. Images are at the same positions as the boxed areas in hematoxylin and eosin (H&E) staining of serial sections. Scale bars, 20  $\mu$ m. (D) Number of total lung cells after dissociation from 4-week-old (gray and black bars) and 24-week-old (pale red and red bars) female BALB/c mice following intranasal inoculation with QHmusX or mock infection (DMEM) at 3 days p.i. ( $n=4$ ). (E) Flow cytometric analysis of lung cells at 3 days p.i. Positive ratios of lymphocytes, neutrophils, eosinophils, and alveolar macrophages (alveolar M) in lung cells are shown. Each dot represents data from an individual animal ( $n=4$ ). \* $P < 0.05$ , \*\* $P < 0.01$ , \*\*\* $P < 0.001$ , and \*\*\*\* $P < 0.0001$  by Dunn's multiple comparison test following the Kruskal-Wallis test.

lymphocytes were observed in the lesions of 4-week-old mice, but very few of these were observed in those of 24-week-old mice. On day 3 p.i., focal inflammatory infiltrations of CD3<sup>+</sup> lymphocytes with a few viral antigen-positive cells were observed around bronchioles and alveoli in 4-week-old mice. However, a lack of epithelia in the bronchiole and many viral antigen-positive cells were observed, with many Iba-1<sup>+</sup>-activated macrophages and some CD3<sup>+</sup> lymphocytes, in 24-week-old BALB/c mice (Fig. 3B). At 10 days p.i., 4-week-old mice showed changes indicative of repair, with aggregation of CD3<sup>+</sup> lymphocytes (Fig. 3C). On the other hand, moribund 24-week-old mice showed diffuse alveolar damage, with infiltration of Iba-1<sup>+</sup>-activated macrophages. To compare the differences in cellular responses in the murine lung in more detail, flow cytometry analysis was conducted using whole lungs of mock- or QHmusX-infected 4- and 24-week-old BALB/c mice on day 3 p.i. (Fig. 3, D and E). The total number of cells in the lung tended to be lower in the 24-week-old control mice than in the 4-week-old control mice (Fig. 3D). In control mice, the ratio of CD4<sup>+</sup> cells was significantly higher in the lungs of 24-week-old mice than in those of the 4-week-old mice (Fig. 3E). The changes in cell proportion after infection were similar

in 4- and 24-week-old mice, except for CD19<sup>+</sup>CD138<sup>+</sup> plasma-blasts and neutrophils. The ratio of both CD4<sup>+</sup> and CD8<sup>+</sup> T cells, CD19<sup>+</sup> B cells, eosinophils, and alveolar macrophages were reduced after infection, whereas the ratio of CD4<sup>+</sup> T<sub>H</sub>1 cells expressing the T<sub>H</sub>1-specific T box transcription factor (T-bet), CD4<sup>+</sup> T<sub>H</sub>17 cells expressing the retinoic acid receptor-related orphan receptor  $\gamma$ t (ROR $\gamma$ t), and NK1.1<sup>+</sup> cells increased in both groups. QHmusX-infected 24-week-old mice showed greater reduction in the ratio of CD4<sup>+</sup> T cells, CD8<sup>+</sup> T cells, CD19<sup>+</sup>CD138<sup>+</sup> plasmablast, and eosinophils in lungs than 4-week-old mice. On the other hand, the ratio of CD4<sup>+</sup> T<sub>H</sub>1 cells expressing T-bet and neutrophils was significantly higher in QHmusX-infected 24-week-old mice. These data indicate that neutrophils, natural killer (NK) cells, T<sub>H</sub>1, and T<sub>H</sub>17 mainly contribute immunopathology in the lungs of 24-week-old mice during early stage after the infection.

Electron microscopy analyses were also performed using lung samples from 24-week-old animals at days 1 and 4 p.i. ( $n = 2$ ) (Fig. 4). In the bronchioles, many degenerated club cells had large numbers of viral particles in the cytoplasm and on the cell surface, but this was not observed in brush cells on day 1 p.i. Some degenerated type II

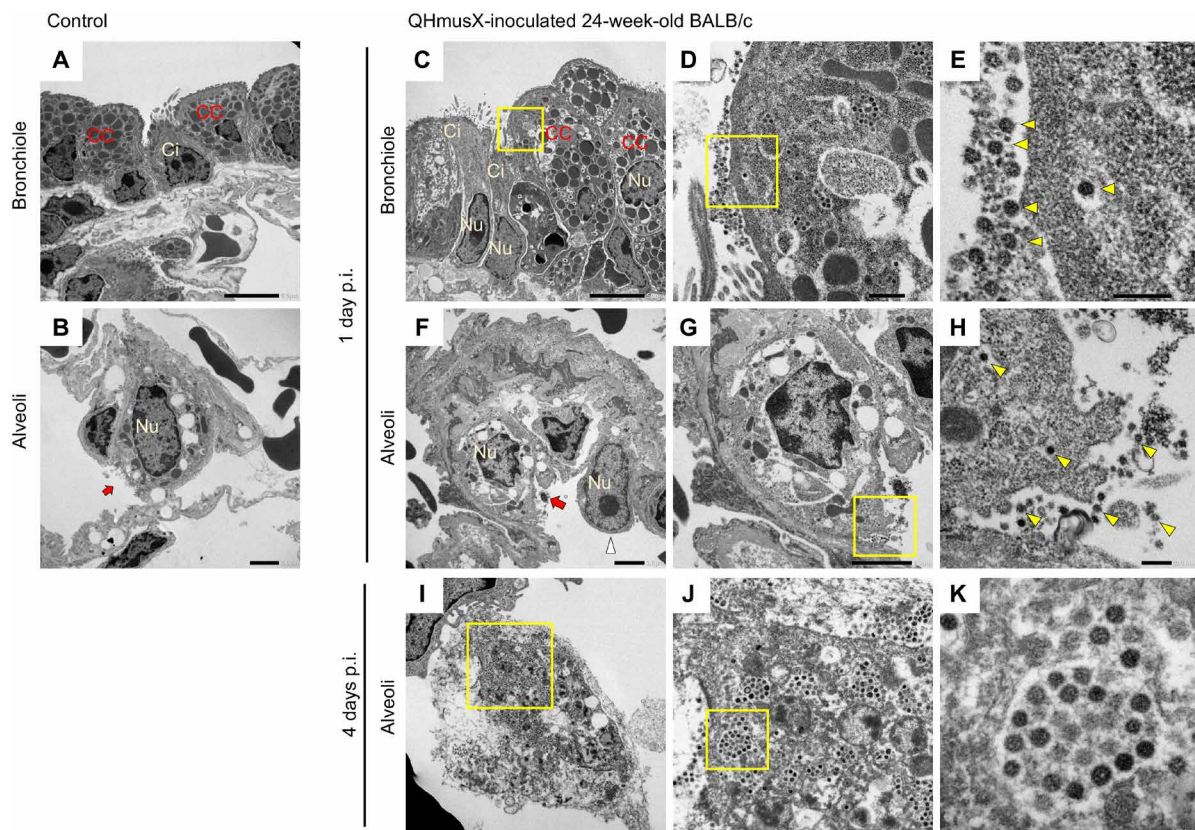


**Fig. 4. Electron microscopy images of viral particles in the bronchioles and alveolar areas of 24-week-old BALB/c mice inoculated with QHmusX.** (A and B) Normal cells in the bronchiole and alveoli from a healthy 24-week-old BALB/c mouse. (C to H) Bronchiolar epithelium (C to E) and type II alveolar epithelium (F to H) on day 1 p.i. (I to K) A degenerated cell with vacuoles containing numerous viral particles in the alveoli on day 4 p.i. Scale bars, 5  $\mu$ m (A and C), 2  $\mu$ m (B, F, G, and I), 500 nm (D and J), 200 nm (E and H), and 100 nm (K). CC, club cell; Ci, ciliated epithelial cell; Nu, nucleus. (A) Club cells with large, ovoid electron-dense granules are nonciliated epithelial cells. A few ciliated epithelial cells were also observed in the terminal bronchioles. (B) A columnar alveolar lining cell with a microvillous surface (arrow) is a type II alveolar pneumocyte. (C) Degenerated club cells in the bronchioles with small vacuoles in the cytoplasm. (D) A higher-magnification image of the boxed area in (C). (E) Higher-magnification image of the boxed area in (D). Many viral particles can be observed (yellow arrowheads). (F) Vacuolar degeneration of type II alveolar epithelia. A white arrowhead and a red arrow indicate type I and type II alveolar epithelia, respectively. (G and H) Higher-magnification images of the type II alveolar epithelium in (F). (H) A higher-magnification image of the boxed area in (G). Viral particles are found (yellow arrowheads). (I) A degenerated alveolar pneumocyte on day 4 p.i. (J and K) Higher-magnification images of the degenerated cell in (I) and (J), respectively.

pneumocytes also contained viral particles in the cytoplasmic vesicle and on the cell surface, but less than that in club cells. On day 4 p.i., numerous vesicles containing many viral particles were observed in degenerated pneumocytes in the alveolar area. This observation indicates that the initial replication site in the murine lung was club cells in the bronchioles and type II pneumocytes in the alveoli after intranasal inoculation with the mouse-passaged SARS-CoV-2 strain, QHmusX.

In addition, we evaluated the susceptibility to infection and age dependency of disease outcomes of inbred mice using  $T_{H1}$ -prone C57BL/6 and  $T_{H2}$ -prone BALB/c mice infected with  $2.3 \times 10^4$  TCID<sub>50</sub> of QHmusX (52LD<sub>50</sub>; more than 10LD<sub>100</sub> in 24-week-old BALB/c mice) ( $n = 6$ ) (fig. S5). Four-week-old C57BL/6 mice did not show any clinical symptoms or weight loss; in addition, 11-week-old, and even 24-week-old, C57BL/6 mice showed transient weight loss without any respiratory symptoms within 3 days p.i., and all recovered (fig. S5A, top). On the other hand, 4- and 11-week-old BALB/c mice showed transient weight loss within 3 days p.i., and all survived, while 24-week-old BALB/c mice were moribund (fig. S5A, bottom). On the basis of the clinical symptoms and viral kinetic studies using BALB/c mice in Figs. 2 and 3, comparative studies in the inbred mice were conducted at 3 days p.i. for viral titers and cytokine levels in the lungs. Higher viral titers were observed in the lungs of mice from BALB/c groups than in those from C57BL/6 groups at 3 days p.i. (fig. S5B). Levels of proinflammatory chemokines and cytokines, including MCP-1, RANTES, MIG, IFN- $\gamma$ , IL-12 (p40), IL-1 $\alpha$ , TNF- $\alpha$ , MIP-1 $\alpha$ , and IFN- $\gamma$ -inducible protein 10 (IP-10), were higher in the lungs of BALB/c mice than in those of C57BL/6 mice at 3 days p.i. (fig. S5C). IL-6 levels were high in the lungs of 24-week-old BALB/c mice. Eotaxin and IL-13 levels were high in C57BL/6 mice. These results show that the QHmusX strain is more highly pathogenic in BALB/c mice than in C57BL/6 mice.

We also examined whether the sex of the mice affected susceptibility to infection and disease outcomes in C57BL/6 and BALB/c mice infected with  $2.3 \times 10^4$  TCID<sub>50</sub> of QHmusX (52LD<sub>50</sub>; more than 10LD<sub>100</sub> in 24-week-old BALB/c mice) ( $n = 6$ ) (fig. S6). Both female and male 17-week-old BALB/c mice exhibited severe body weight loss and respiratory symptoms and then became moribund, whereas five of six male BALB/c mice recovered within 7 days p.i. (fig. S6A). On day 3 p.i., no significant difference between the titers in the lungs of male and female BALB/c mice was observed (fig. S6B). However, the levels of proinflammatory chemokines and cytokines including MCP-1, RANTES, IL-12 (p70), IL-1 $\alpha$ , and IL-1 $\beta$  were higher in the lungs of female BALB/c mice, whereas the levels of MIG, keratinocyte-derived chemokines (KC), IP-10, and IL-13 were lower at 3 days p.i. (fig. S6C). Conversely, both male and female C57BL/6 mice showed transient weight loss without any respiratory symptoms within 3 days p.i., and all recovered (fig. S6D). There were significant differences in the percent changes in initial body weights between female and male C57BL/6 from 3 to 5 days p.i. However, no significant difference was observed in viral titers or cytokine levels in the lungs from C57BL/c mice at 3 days p.i. (fig. S6, E and F). These results indicate that sex affected the outcomes of adult BALB/c.

### Establishment of an experimental model to challenge BALB/c mice immunized with the SARS-CoV-2 S protein ectodomain

Next, we evaluated the utility of this animal model for investigating vaccine efficacy and vaccine-associated enhanced respiratory disease upon infection with mouse-passaged SARS-CoV-2. The recombinant

S protein ectodomain of SARS-CoV-2 (S-ect), which was prepared using a mammalian cell expression system, was used as an immunogen (Fig. 5A). Alum was used as a  $T_{H2}$  adjuvant, and TLR agonists were used as a  $T_{H1}$ - $T_{H2}$  balanced adjuvant, according to a previous study (11). Ten micrograms of S-ect with 1 mg of alum (referred to as S-ect + alum) and 10  $\mu$ g of S-ect with TLR agonists (referred to as S-ect + TLR), consisting of 1  $\mu$ g of lipopolysaccharide (Sigma-Aldrich, St. Louis, MO), 2.5  $\mu$ g of polyinosinic-polycytidylic acid [poly(I:C)] (Invitrogen, San Diego, CA), and 0.1  $\mu$ g of polyuridylic acid [poly(U)] (Invitrogen), were administered by intramuscular injection in a 50- $\mu$ l volume at 2-week intervals. The immunization and challenge schedule is shown in Fig. 5B. After the two immunizations of adult BALB/c mice (20 weeks old at the initial immunization) at 2-week intervals, SARS-CoV-2 S protein-specific immunoglobulin G 2a (IgG2a) and IgG1 levels were measured by enzyme-linked immunosorbent assay (ELISA) (Fig. 5C). The lower IgG2a/IgG1 ratio in the S-ect and S-ect + alum groups suggested that the  $T_{H2}$ -shifted immune response was stronger in the S-ect and S-ect + alum groups than in the S-ect + TLR group. A high neutralizing antibody titer was detected in the group immunized with S-ect + TLR, but low titers were observed in the groups immunized with S-ect and S-ect + alum (Fig. 5D).

After the experimental infection of adult BALB/c mice (25 weeks old when challenged with infection) with  $2.3 \times 10^4$  TCID<sub>50</sub> of QHmusX, 6 of 10 mice in each group were monitored daily for changes in body weight, and data for survival curves were obtained (Fig. 5, E and F). All BALB/c mice from the control groups, including groups injected with phosphate-buffered saline (PBS), PBS + alum, or PBS + TLR, developed severe acute respiratory illness and became moribund within 6 days p.i. On the other hand, all mice in the group immunized with S-ect + TLR showed no obvious clinical symptoms and survived throughout the observation period (10 days p.i.). The group immunized with S-ect + alum showed transient weight loss with mild clinical symptoms, such as ruffled fur, within 3 days p.i., and recovered until body weight returned to the initial level. All animals from the group immunized with S-ect had respiratory symptoms and weight loss, and only two of six mice survived during the observation period.

### Immune responses and eosinophilic infiltration in the lungs of immunized mice after SARS-CoV-2 challenge

At 3 days after infectious challenge, 4 of 10 mice in each group were euthanized to assess viral titers (Fig. 5G) and cytokine responses in the lungs (Fig. 5H). Viral titers were lower in the group immunized with S-ect + TLR than in other groups. Lower titers were detected in the group immunized with S-ect + alum than those in the control group, but these titers were higher than those in the group immunized with S-ect + TLR. Proinflammatory cytokines and chemokines, including IL-6, MCP-1, and KC, were produced at higher levels in the control groups than in the immunized groups. Levels of the proinflammatory chemokines MIP-1 $\alpha$ , IP-10, and MIG were lower, and levels of the  $T_{H1}$ -related cytokines and chemokines IL-2, IL-13, and eotaxin were higher in the group immunized with S-ect + TLR than in the other groups. Inflammatory cytokines TNF- $\alpha$ , IL-1 $\alpha$ , and IL-1 $\beta$ , as well as  $T_{H2}$ -related cytokines and chemokines, including IL-4 and IL-5, were produced at high levels in groups immunized with either S-ect or S-ect + alum. We next conducted transcriptome analysis by extracting RNA from the same lung homogenates described in Fig. 5G at 3 days p.i. Multidimensional scaling analysis

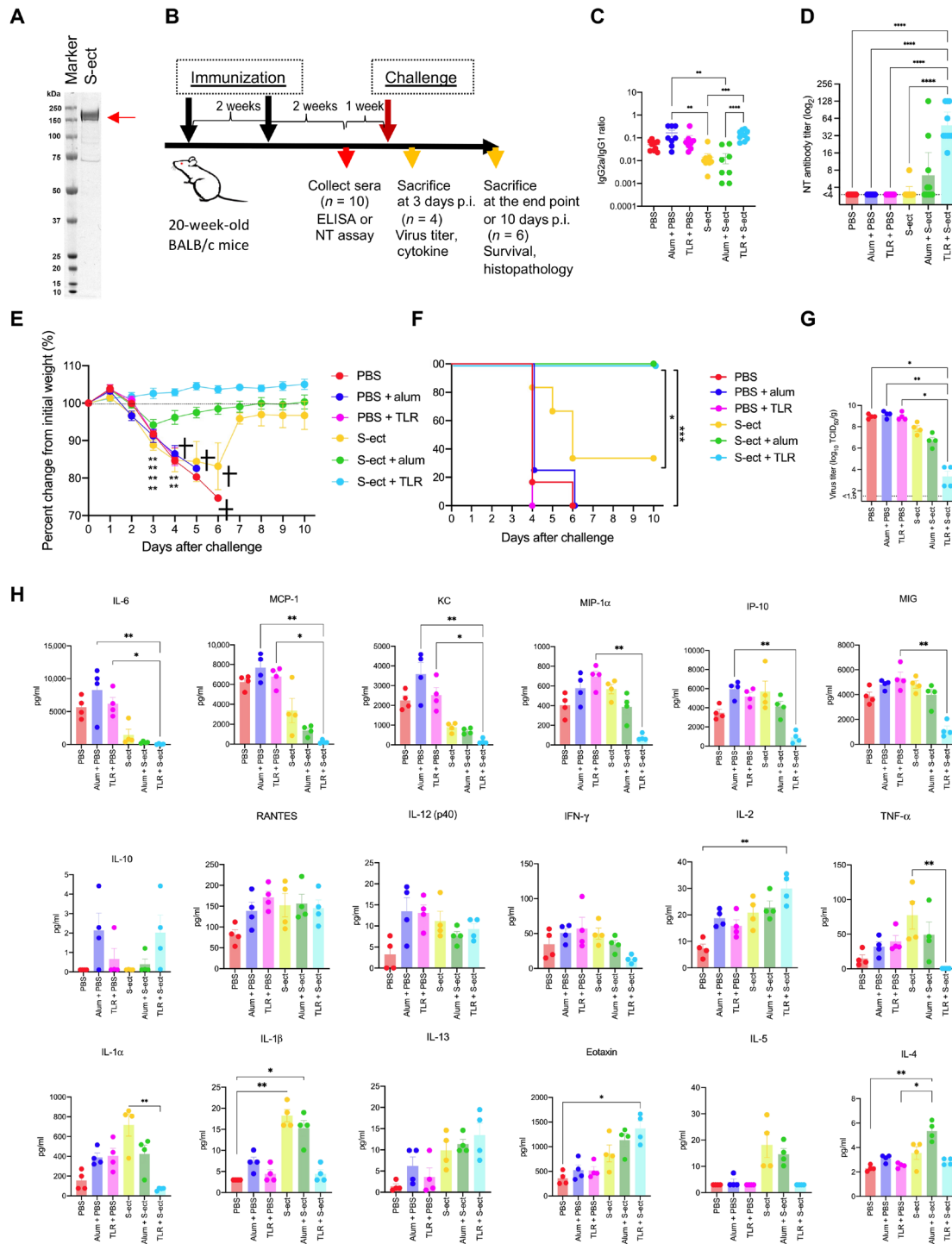


**Fig. 5. Establishment of an experimental model to challenge BALB/c mice immunized with the adjuvanted SARS-CoV-2 S-ect with mouse-passaged SARS-CoV-2.**

(A) SDS-polyacrylamide gel electrophoresis followed by Coomassie blue staining using a purified recombinant SARS-CoV-2 monomeric S-ect with an expected molecular weight of 137 kDa. (B) Vaccine and challenge infection schedule using 6-month-old BALB/c mice and QHmusX. (C) SARS-CoV-2 S protein-specific IgG2a/IgG1 ( $T_{H1}/T_{H2}$ ) ratios in the sera at 2 weeks after the second immunization ( $n = 10$ ). (D) Serum neutralizing titers (NTs) after the second immunization. Samples were from the same experiment as those in (C). The dashed line indicates the limit of detection ( $<4$ ) ( $n = 10$ ). (E) Body weight changes after infectious challenge with QHmusX. \*\* $P < 0.01$ . Tukey's multiple comparisons test was used to compare the results with those from the S-ect + TLR group ( $n = 6$ ). (F) Survival curves after infectious challenge with QHmusX from the same animals as in (E). The log-rank (Mantel-Cox) test was used to compare survival curves with that of the S-ect + TLR group ( $n = 6$ ). \* $P < 0.05$  and \*\*\* $P < 0.001$ . (G) Viral titers in the lungs of immunized mice after QHmusX challenge at 3 days. The assays were performed using a unicate sample for each animal ( $n = 4$ ). (H) Cytokine and chemokine levels in the lungs of immunized or nonimmunized animals at 3 days after infection with QHmusX. Samples were from the same experiment as those in (G) ( $n = 4$ ). (C, D, G, and H) \* $P < 0.05$ , \*\* $P < 0.01$ , \*\*\* $P < 0.001$ , and \*\*\*\* $P < 0.0001$  by Dunn's multiple comparison test following the Kruskal-Wallis test.

showed that the group immunized with S-ect + TLR was distinct from the other two immunized groups (S-ect and S-ect + alum) and the three naïve groups (PBS, PBS + alum, and PBS + TLR) (Fig. 6A). Hierarchical clustering analysis was used to graphically represent the similarity in gene expression patterns between samples (Fig. 6B). The 5330 genes satisfied the conditions of an absolute fold change of  $\geq 1.5$  and a negative binomial Wald test raw  $P < 0.05$  for at least one of the comparison pairs. A heatmap of the 57 genes (more than 15-fold up-regulated or down-regulated compared with the control PBS group), which were associated with external stimulus response, innate immune response, defense response to virus, response to type I IFN, type II IFN signaling, inflammatory response, apoptotic process, and adaptive immune response, revealed differential gene expression in the six groups (fig. S7). In the three naïve groups, gene expression related to immunity, inflammation, and apoptosis was much higher. The expression of type II IFN signaling (*Ifit2*, *Cxcl10*, *Isg15*, and *Cscl9*) and C-X-C motif chemokine receptor 3 (CXCR3) chemokine receptor binding-related genes (*Cxcl10*, *Cxcl11*, and *Cxcl9*) was high in the naïve groups and S-ect and S-ect + alum groups, but not in the S-ect + TLR group. Overall, substantially different immune responses to SARS-CoV-2 infection occurred in the group immunized with S-ect + TLR, the other two immunized groups, and the three naïve groups at 3 days p.i.

We next performed flow cytometry analysis of lung cells after challenge infection in the whole lung of the control PBS, S-ect + alum, and S-ect + TLR mice on day 3 p.i. (fig. S8, A and B). The total number of cells in the lung tended to be lower in the S-ect + TLR mice than in the PBS and S-ect + alum mice (fig. S8C). The changes in the proportions of cells after infection were similar in both immunized groups, but there was a higher ratio of CD4<sup>+</sup> T cells including those expressing GATA binding protein 3 (GATA3) and CD4<sup>+</sup> Th17 cells expressing RORyt in the S-ect + TLR group (fig. S8D). NK1.1<sup>+</sup> cell ratio that was low and high ratio of alveolar macrophage was observed in the S-ect + TLR group. Histopathological analysis revealed mononuclear cells around blood vessels in the control group and vessel wall-attached mononuclear and eosinophil cells (fig. S8E, asterisk) infiltrating around blood vessels in the lungs of S-ect + alum mice at 3 days p.i. In the S-ect + TRL mice, mononuclear cells and a few eosinophils were observed around blood vessels.

We also examined histopathology in the lungs to investigate vaccine-related eosinophilic immunopathology after SARS-CoV-2 infection (Fig. 6, C to F). In control mice, diffuse alveolar damage with viral replication was observed, with severe edema around blood vessels at the humane end point (Fig. 6C). Very slight inflammatory infiltration with neutrophils and mononuclear cells, but very few eosinophils, was seen in the lesions. On the other hand, predominantly eosinophilic infiltration with a few viral antigens was observed around the bronchioles and in the alveoli of a moribund mouse from the group immunized with S-ect (Fig. 6D). Mice in the groups immunized with S-ect or S-ect + alum that survived exhibited eosinophilic infiltration surrounding the bronchioles and blood vessels of the lungs, but this was not observed in the group immunized with S-ect + TLR on day 10 p.i. (Fig. 6E). The number of eosinophils was significantly lower in the group immunized with S-ect + TLR than those in the groups immunized with S-ect (Fig. 6F). These results indicate that a Th2-shifted immune response and insufficient neutralizing antibody levels induced eosinophilic immunopathology after infection with mouse-passaged SARS-CoV-2, similar to results from SARS-CoV mouse models in previous studies (10, 11).

In addition, we performed a serum transfer experiment in which sera from animals with high levels of neutralizing antibody to QHmusX (1:128) induced by S-ect + TLR immunization was transferred into PBS and S-ect + alum mice (fig. S9A). After intraperitoneal injection with the antibody containing neutralizing antibody to QHmusX or normal sera into PBS and S-ect + alum mice, QHmusX was inoculated into these animals. The S-ect + alum mice showed low levels of neutralizing antibody at 2 week after the second immunization (fig. S9B). At 3 days p.i., there was no significant difference in viral titers between the four groups of mice (fig. S9C). All mice from the normal sera-injected control groups (group I in fig. S9) developed severe acute respiratory illness and became moribund within 6 days p.i. (fig. S9D). On the other hand, three of four mice injected with the serum from S-ect + TLR-immunized mice (group II in fig. S9) showed transient weight loss within 3 days p.i. but survived throughout the observation period (10 days p.i.). The normal sera-injected animals immunized with S-ect + alum (group III in fig. S9) showed transient weight loss within 3 days p.i. Three of four animals recovered until 7 days p.i. All S-ect + alum-immunized animals injected with the serum (group IV in fig. S9) showed transient body weight loss until 3 days p.i. but recovered quickly. However, both groups III and IV showed eosinophilic infiltration surrounding the bronchiole and blood vessels (fig. S9, E and F). Thus, neutralizing antibody alone did not improve the vaccine-induced eosinophilic immunopathology. These data suggest that T cells and other immune cells may participate in vaccine-associated enhanced respiratory disease in this model. Overall, we established a lethal mouse model that allows the evaluation of vaccine efficacy and vaccine-associated enhanced respiratory disease after infection with mouse-passaged SARS-CoV-2.

### Insufficient neutralizing antibody levels induced eosinophilic immunopathology after reinfection

Last, we also examined the effect of prior infection with SARS-CoV-2 by reinfecting mice to evaluate whether enhanced immunopathology occurred after reinfection. After experimental infection with the original QH-329-037 isolate or the mouse-passaged QHmusX strain, animals that survived were examined for seroconversion and challenged again with QHmusX infection (fig. S10A). Seroconversion was observed in all 4-week-old BALB/c mice inoculated with QHmusX, but only in two of six 6-month-old BALB/c mice inoculated with QH-329-037 (fig. S10B). After reinoculation with QHmusX, control mice (8 weeks old at the second inoculation; referred to as 8w; DMEM-QHmusX in fig. S7C) and young mice preinoculated with QH-329-037 (referred to as 8w; QH329-QHmusX in fig. S10C) showed transient weight loss within 3 days p.i., but young mice preinoculated with QHmusX did not (referred to as 8w; QHmusX-QHmusX in fig. S10C). Adult BALB/c mice preinoculated with QH-329-037 (referred to as 7m; QH329-QHmusX in fig. S10C) showed transient weight loss; however, no animals developed lethal respiratory illness after reinoculation with QHmusX. Histopathological analysis revealed that a prior infection was effective in averting severe damage of the pulmonary tract after inoculation with QHmusX (fig. S10D). Obvious inflammatory infiltration, with eosinophils around the bronchioles, was observed in 7-month-old animals from the QH329-QHmusX group (fig. S10, D and E).

### DISCUSSION

For rapid response to COVID-19, including research for evaluation of medical countermeasures, Dinnon *et al.* (25) produced mouse-adapted

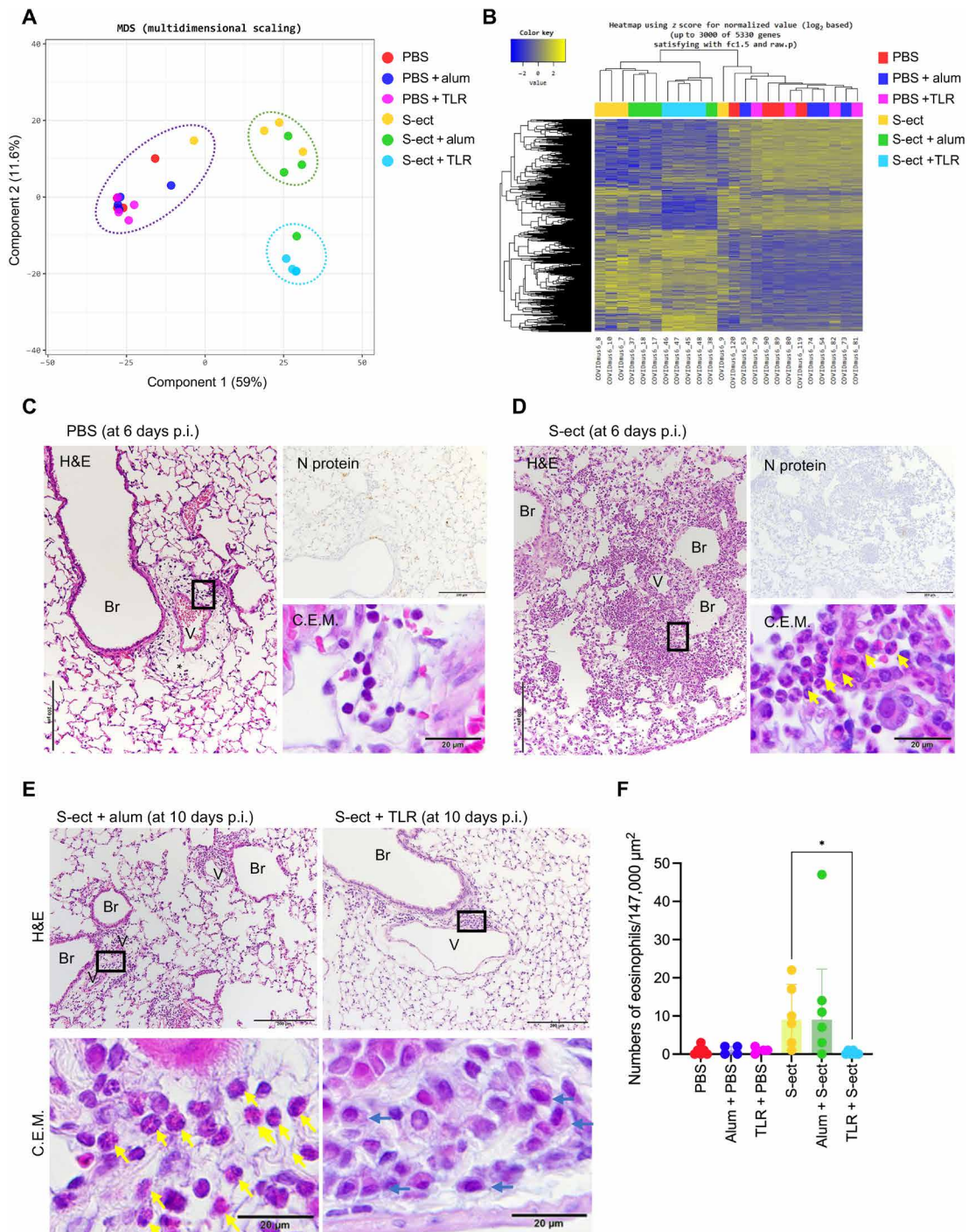


**Fig. 6. Immune responses and eosinophilic infiltration in the lungs of immunized mice after SARS-CoV-2 challenge.** Samples were from the same experiment as those in Fig. 4. (A) Multidimensional scaling (MDS) analysis of RNA sequencing data from 24 murine lung samples in the six groups at 3 days after infectious challenge with QHmusX. (B) Representative heatmap of gene transcripts whose expression was significantly altered in the six groups. The heatmap contains up to 3000 of the 5330 genes that satisfied the conditions of a  $\log_2$  fold change of  $>1.5$  and a raw  $P < 0.05$  in one-way hierarchical clustering analysis using z scores for normalized values ( $\log_2$  based). (C to E) Representative histopathological findings from the mice with the highest eosinophilic infiltration were detected by H&E staining and eosinophilic staining using the combined eosinophil–mast cell stain (C.E.M.) kit. Yellow arrows indicate representative eosinophils. Results from the PBS-pretreated control (C) and mice immunized with S-ect (D) on day 6 and mice immunized with S-ect + alum or S-ect + TLR on day 10 after infectious challenge (E). H&E, low magnification of H&E staining; IHC, immunohistochemistry for viral antigens. Scale bars, 200  $\mu\text{m}$ . C.E.M., high magnification of eosinophilic staining in the boxed area shown in H&E-stained serial sections. Scale bars, 20  $\mu\text{m}$ . V, blood vessel. (F) Number of eosinophils per lung section ( $n = 4$  or 6) at the humane end point or 10 days after challenge. Five 147,000- $\mu\text{m}^2$  regions around the pulmonary bronchioles of each mouse were counted at  $\times 600$  magnification. Each circle shows the median value from an individual animal. \* $P < 0.05$  by Dunn's multiple comparison test following the Kruskal-Wallis test.

SARS-CoV-2 by reverse genetics. Remodeling the interaction between the SARS-CoV-2 S protein and murine ACE2 revealed that the amino acid position 498 in the receptor binding site of the S protein of SARS-CoV-2 was uniquely divergent. The Q498Y and P499T mutations were introduced into the SARS-CoV-2 S gene using reverse genetics, and the recombinant virus SARS-CoV-2 MA (mouse-adapted SARS-CoV-2) was recovered. The MA virus could use murine ACE2 for entry into cells and replicate in the respiratory tracts of BALB/c mice; however, these animals showed only mild-to-moderate disease, even in 1-year-old adult BALB/c mice (25). Next, the MA virus was passaged 10 times by transferring lung homogenate from BALB/c mice, and the virulent MA10 strain was obtained by plaque purification (30). The MA10 virus had five additional nonsynonymous mutations: T285I in nonstructural protein 4 (nsp4), K2R in nsp7, E23G in nsp8, Q493K in S protein, and F7S in ORF6. Furthermore, Wang *et al.* (31) serially passaged a human isolate, SARS-CoV-2/HRB26/human/2020/CHN (HRB26), in BALB/c mice using a mixture of nasal turbinate and lung homogenate (31). They also found two nonsynonymous mutations, Q498H and N969S, and a five-amino acid deletion (675QTQTN679) in the S protein in this mouse-passaged SARS-CoV-2 strain, HRB26M. Infection with the HRB26M strain induced transient weight loss, but both young and adult BALB/c mice recovered. In this study, we demonstrated that a SARS-CoV-2 isolate of European lineage (D614G), QH-329-037, could be serially passaged in mice *in vivo* using lung lavage from young BALB/c mice. The mouse-passaged strain differed from the original mouse strain in four amino acid substitutions. QHmusX rapidly acquired a nonsynonymous Q498H mutation in the S protein (at the initial passage *in vivo*), and we confirmed that binding affinity was altered. We did not determine which position was more important for enhanced virulence in BALB/c mice, but position 498 in the receptor binding domain of S protein in SARS-CoV-2 is a critical site for mouse adaptation. In addition, a mixture of single-nucleotide polymorphisms was detected at the R203K position in the N protein of QH-329-037, and one of these, 203K, was selected immediately during mouse passages. On the other hand, two nonsynonymous mutations were detected in nsp8 and were substituted at the second (in nsp8; K61R) and sixth (in nsp8; S8F) passages. Coronavirus depends on an RNA-dependent RNA polymerase complex for replication of its genome and transcription of its genes. Both nsp8 and nsp7 are cofactors that greatly stimulate nsp12 RNA-dependent RNA polymerase activity (32, 33). The two substitutions in nsp8 might affect viral proliferation in mice. After VeroE6/TMPRSS2 cell propagation, two sites with a single-nucleotide polymorphism appeared in nsp8 (nsp8; T89I) and nsp10 (nsp10; T58I), which appeared to be related viral replication in the cells. In general, we used a SARS-CoV-2 isolate of European lineage (D614G) for mouse passages. Our study suggests that the Q498H mutation in S protein facilitates coronavirus adaptation in mouse and two nonsynonymous mutations in nsp8 affect viral replication in mice.

The QHmusX strain, passaged 10 times in mice, induced different outcomes in an age-dependent fashion: severe respiratory illness developed in adult female BALB/c mice (more than 17 weeks old), but not in young female BALB/c mice (less than 11 weeks old). Viral kinetics, immune response analyses, pathological studies, and flow cytometry analysis suggest that the antiviral response in early stages and immunopathology against SARS-CoV-2 are crucial to outcomes in female BALB/c mice after infection. Neutrophils, NK cells,  $T_{H}1$ , and  $T_{H}17$  contributed immunopathology in early stage

after the infection. Moribund adult female BALB/c mice showed severe pulmonary edema and diffuse alveolar damage accompanied by viral replication. In addition, no C57BL/6 mice with a  $T_{H}1$ -shifted immune response developed any severe respiratory illness after inoculation with QHmusX. The outcomes of adult BALB/c and C57BL/6 mice differed according to their sex. Male and female BALB/c mice have been reported to have very different susceptibilities to myocarditis following coxsackievirus B3 experimental infection (34). The  $T_{H}2$  cell phenotypic response induced in female BALB/c mice resulted in better humoral immune responses than in male BALB/c mice, but the predominant  $T_{H}1$  response in male BALB/c mice resulted in myocarditis after coxsackievirus B3 infection. Conversely, in our mouse model, the  $T_{H}2$ -dominant response in female BALB/c mice resulted in a poor outcome after mouse-adapted SARS-CoV2 infection. These results indicate that an imbalance in  $T_{H}1$  and  $T_{H}2$  responses ( $T_{H}1 < T_{H}2$ ) might contribute to the excessive and rapid proinflammatory cytokine response, including IL-1 and TNF- $\alpha$ , during SARS-CoV-2 infection, similar to that observed for SARS-CoV (27). Histopathological findings, such as excessive pulmonary edema and diffuse alveolar damage, were very similar to those in our previous murine model for SARS-CoV using adult BALB/c mice (27, 35). Both the mouse-passaged SARS-CoV, F-musX, and the mouse-passaged SARS-CoV-2, QHmusX, strains infected and replicated in pulmonary epithelial cells of bronchioles and the alveolar area and in type II pneumocytes on day 1. On days 2 and 3 p.i., alveoli and macrophages were positive for viral antigen, but less viral antigen was observed in bronchioles (27). The level of antigen staining was less than would be expected for a lethal infection. However, very few intact pneumocytes with/without viral antigens were observed in alveoli, whereas regenerated cells were observed in bronchi. In addition, dead mice showed extensive diffuse alveolar damage with edema, congestion, and hemorrhage in all lung lobes. In sum, both animal models showed very similar terminal histopathology, including massive pulmonary edema and diffuse alveolar damage at the end point.

In this study, electron microscopy analysis identified that club cells (previously referred to as "Clara" cells) were the most relevant site for viral infection and replication in the murine lung during early stages after intranasal inoculation with mouse-passaged SARS-CoV-2. Club cells have many functions in the bronchioles, including secreting proteins with roles in the extracellular fluid lining distal airways and regulating its content, acting as a progenitor for other bronchial cells, producing surfactant, metabolizing toxic substances, and regulating the pulmonary immune system (36). Thus, viral infection in club cells might notably affect immunopathology during SARS-CoV-2 infection. Further research is necessary; however, this finding contributes to a better understanding of pathogenesis in early stages of SARS-CoV-2 infection.

In a rapid response to the COVID-19 pandemic, several SARS-CoV-2 vaccine candidates were developed using a variety of technology platforms. On the basis of experience from developing SARS-CoV and MERS-CoV vaccines (37, 38), some vaccine developers selected nucleic acid vaccines, which induce  $T_{H}1$ -predominant responses and allow for rapid manufacturing of SARS-CoV-2 vaccines (39–41). On the other hand, inactivated vaccines are a basic platform that has a long history of use for inducing protection against pathogen and can easily be produced on a large scale (42, 43). In addition, subunit vaccines are considered highly safe products, because they use antigenic components without the need to introduce viral particles (38, 43). Thus, it is necessary to consider several vaccine platforms for SARS-CoV-2 vaccines.

In previous SARS-CoV and MERS-CoV studies using murine models, both inactivated and subunit vaccines have the potential to enhance respiratory disease associated with eosinophilic immunopathology after infectious challenge (6, 7, 10, 11, 20, 21, 44). In this study, we provide evidence that disease enhancement associated with eosinophilic immunopathology was induced by T<sub>H</sub>2-shifted immune responses and inadequate neutralizing antibody levels in BALB/c mice immunized with S-ect and S-ect + alum after challenge with murine-passaged SARS-CoV-2. Similar to the previous study using the SARS-CoV mouse model, eosinophilic immunopathology was avoided using TLR agonists as adjuvants, which induced a balanced T<sub>H</sub>1 and T<sub>H</sub>2 immune response (10, 11, 20). Differences in the gene expression of CC chemokine receptor Ccr1 (eosinophil and monocyte migration) and Ccr5 (decreased eosinophilia and airway hyperreactivity) were observed between immunized groups and naïve groups. Deming *et al.* (8) demonstrated that injection with a neutralizing antibody alone did not improve vaccine-induced immunopathology. In our study, the high neutralizing antibody induced by S-ect + TLR alone did not improve vaccine-induced eosinophilic immunopathology in S-ect + alum-immunized BALB/c mice. These results indicate that T cells and other immune cells may also participate in vaccine-associated enhanced respiratory disease in mouse models.

Eosinophilic infiltration around the bronchioles was also observed in adult BALB/c mice inoculated with the original isolate after the second infection with QHmusX. Several SARS-CoV-2 reinfection cases of SARS-CoV-2 have been reported (45, 46). The possibility of enhanced immunopathology at the second infection is an ongoing discussion. Results from this murine model suggest that the possibility of reinfection with a different variant of SARS-CoV-2, as well as inadequate neutralizing antibody levels, might contribute to eosinophilic immunopathology during reinfection.

For preclinical research for SARS-CoV-2 vaccine candidates, inbred mice represent the most appropriate animal model because of convenience: size, handling, cost, maintenance, reproducibility, and sufficient research tools (i.e., immunology and anatomy). In addition, study designs for assessing vaccine-associated enhanced respiratory disease have been well established in SARS-CoV and MERS-CoV studies (6–11, 19–21). While this animal model has some limitations (only the mouse-adapted SARS-CoV-2 strain can be used), we believe that this animal model will contribute to the accelerating COVID-19 vaccine development.

Together, we established a lethal BALB/c mouse model to evaluate vaccine-associated enhanced respiratory disease after infection with mouse-passaged SARS-CoV-2. The data also suggest the potential for vaccine-associated enhanced respiratory disease in humans immunized with SARS-CoV-2 candidate vaccines, similar to observations in SARS-CoV and MERS-CoV studies. During and after clinical trials for SARS-CoV-2 vaccine candidates, continuous monitoring is needed. This animal model can contribute to basic studies on pathogenesis and to the selection of vaccine strategies and adjuvants.

## MATERIALS AND METHODS

### Ethics statements

All procedures involving cells and animals were conducted in a bio-safety level 3 (BSL3) laboratory. Experiments using recombinant DNA and pathogens were approved by the Committee for Experiments using Recombinant DNA and Pathogens at the National Institute of Infectious Diseases, Tokyo, Japan. All animal experiments were

approved by the Animal Care and Use Committee of the National Institute of Infectious Diseases in Japan (approval nos. 119164, 120042, 120070, 121075, and 121079), and all experimental animals were handled in BSL3 animal facilities according to the guidelines of this committee (approval nos. 19-53, 20-39, 20-31, 21-27, and 21-28). All animals were housed in a facility certified by the Japan Health Sciences Foundation.

### Cells and viruses

VeroE6/TMPRSS2 cells purchased from the Japanese Collection of Research Bioresources Cell Bank (the National Institute of Biomedical Innovation, Health, and Nutrition, Osaka, Japan) were used in this study (47). Cells were cultured in DMEM, low glucose (Sigma-Aldrich, St. Louis, MO), containing 10% fetal bovine serum (FBS), penicillin G (50 IU/ml), and streptomycin (50 µg/ml) (10DMEM). SARS-CoV-2 human isolates were prepared and provided by S. Matsuyama and M. Takeda (Department of Virology III, National Institute of Infectious Diseases, Japan) (47). Stocks of the WK-521 (accession no. EPI\_ISL\_408667) isolate and QH-329-037 (accession no. EPI\_ISL\_529135) were propagated and titrated on VeroE6/TMPRSS2 cells in DMEM containing 2% FBS, penicillin G (50 IU/ml), and streptomycin (50 µg/ml) (2DMEM). Viral infectivity titers were expressed as TCID<sub>50</sub> per milliliter in VeroE6/TMPRSS2 cells and were calculated according to the Behrens-Kärber method. Work with infectious SARS-CoV-2 was performed under BSL3 conditions.

### Study design

Mouse-passaged virus were produced using an SARS-CoV-2 isolate similar to the one used in a previous SARS-CoV study (27). Three BALB/c mice were intranasally infected with the SARS-CoV-2 QH-329-037 strain for the first passage, and three naïve mice were intranasally administered 30 µl of lung lavage from the three mice in the previous passage for all following passages. The mice were euthanized on day 3 p.i., and lung lavage was collected from lungs washed three times with 0.1% bovine serum albumin, penicillin G (20 IU/ml), streptomycin (20 µg/ml), and amphotericin B (1 µg/ml). After 10 passages in mice, SARS-CoV-2 RNA levels and viral loads were estimated in the lung lavage of mice from each passage. Viral stocks were propagated in VeroE6/TMPRSS2 cells.

BALB/c and C57BL/6 mice (4, 11, 17, and 24 weeks old) were purchased from Japan SLC (Shizuoka, Japan) and were maintained in specific pathogen-free facilities. These mice were anesthetized by intraperitoneal injection with a mixture of 0.1 ml/10 g of body weight of 1.0 mg of ketamine and 0.02 mg of xylazine. Animals were then inoculated intranasally with  $1.7 \times 10^6$  or  $2.3 \times 10^5$  TCID<sub>50</sub> (30 µl) of QH-329-037 or  $2.3 \times 10^4$  TCID<sub>50</sub> (30 µl) of QHmusX. LD<sub>50</sub> titers of QHmusX were determined by inoculating groups of seven mice intranasally with serial 10-fold dilutions of virus and were calculated according to the Behrens-Kärber method. Body weight was measured daily for 10 days ( $n = 6$  per group), and animals were euthanized at 6 hours and at 1, 2, 3, 4, and 10 days p.i. to analyze viral replication, cytokine expression, and disease pathology ( $n = 3$  to 6 per group). Clinical signs were observed up until 10 days p.i. All mock-infected mice were inoculated with 2DMEM. The humane end point was defined as the appearance of clinically diagnostic signs of respiratory stress, including respiratory distress and more than 25% weight loss. Animals were euthanized under anesthesia with an overdose of isoflurane if severe disease symptoms or weight loss was observed.

### Immunization and challenge experiments

Twenty-week-old BALB/c mice were vaccinated with 10 µg of recombinant SARS-CoV-2 monomeric S-ect, 10 µg of S-ect with 1 mg of alum, or 10 µg of S-ect with TLR agonists, consisting of 1 µg of lipopolysaccharide (Sigma-Aldrich), 2.5 µg of poly(I:C) (Invitrogen, San Diego, CA), and 0.1 µg of poly(U) (Invitrogen). Vaccines were administered via intramuscular injection in a 50-µl volume at 2-week intervals. Control mice were injected intramuscularly with PBS, with or without 1 mg of alum or TLR agonists. The presence of viral-specific IgG and neutralizing antibodies was confirmed in blood samples obtained from the tail vein at 2 weeks after the second immunization. Three weeks after the boost immunization, mice were inoculated intranasally with QHmusX ( $2.3 \times 10^4$  TCID<sub>50</sub> per mouse) under anesthesia (ketamine-xylazine). After infection, the animals were monitored once a day during the study, and mice were euthanized by isoflurane overdose on day 3 after infection. Viral titers in the lungs were analyzed by microtitration assays.

### RNA extraction and quantification of viral RNA genomes

Viral RNA from each lung lavage at passages 1 to 10 was isolated using the TRIzol Plus RNA Purification Kit (Thermo Fisher Scientific, MA), following the manufacturer's suggested protocol, and quantified by NanoDrop (Thermo Fisher Scientific). Viral RNA quantification of each sample was performed by real-time reverse transcription PCR targeting the N gene of SARS-CoV-2 using the QuantiTect Probe RT-PCR Kit (QIAGEN, Hilden, Germany) with the following primers and probes: NIID\_2019-nCOV\_N\_F2 (5'-AAATTTGGGGAC-CAGGAAC-3'), NIID\_2019-nCOV\_N\_R2 (5'-TGGCAGCTGTG-TAGGTCAAC-3'), and NIID\_2019-nCOV\_N\_P2 (5'-FAM-ATGT CGCGCATTGGCATGGA-BHQ-3') (48). The reaction mixtures were incubated at 50°C for 30 min, followed by incubation at 95°C for 15 min, and thermal cycling, which consisted of 40 cycles of denaturation at 94°C for 15 s, as well as annealing and extension at 60°C for 60 s. This assay was performed on a LightCycler 480 (Roche, Basel, Switzerland).

### Next-generation sequencing

Whole-genome amplification of strain QHmusX was carried out using a modified version of ARTIC Network's protocol for SARS-CoV-2 genome sequencing by replacing some of the primers for multiplex PCR. An NGS library was constructed using the QIAseq FX DNA Library kit (QIAGEN) and sequenced using the NextSeq 500 platform (Illumina, San Diego, CA). NGS reads were mapped to the SARS-CoV-2 Wuhan-Hu-1 reference genome sequence (GenBank accession no. MN908947.3) using the *bwa mem* algorithm (version 0.7.13-r1126) (49), followed by trimming of the primer region with "trim\_primer\_parts.py" ([https://github.com/ItokawaK/Alt\\_nCov2019\\_primers](https://github.com/ItokawaK/Alt_nCov2019_primers)). To determine the nearly full-length genome sequence, the trimmed reads were assembled using SKESA version 2.3.0 (50) or A5-miseq version 20140604 (51). Variant allele frequency analysis of mapping data was performed using VarScan version 2.4.3 (52). The full-genome sequence of strain QHmusX was deposited in the DNA Data Bank of Japan ([www.ddbj.nig.ac.jp/index.html](http://www.ddbj.nig.ac.jp/index.html)) under accession no. LC605054. All short-read sequences were deposited in the DNA Data Bank of Japan [BioProject PRJDB11095, DDBJ Sequence Read Archive (DRA) accession no. DRA011496].

### Histopathology and immunohistochemistry

To obtain animal tissues, mice were anesthetized and perfused with 2 ml of 10% phosphate-buffered formalin, and the lungs, liver,

spleen, kidneys, heart, gastrointestinal tract, salivary glands, and brain tissues were harvested and fixed. Fixed tissues were routinely embedded in paraffin, sectioned, and stained with hematoxylin and eosin (H&E). Eosinophils were identified by Astra Blue/Vital New Red staining, a combined eosinophil–mast cell stain (C.E.M. Stain Kit, Diagnostic Biosystems, Pleasanton, CA). Using slides stained with Astra Blue/Vital New Red, peribronchiolar areas in five 147,000-µm<sup>2</sup> sections were assessed by light microscopy using a DP71 digital camera and cellSens software (Olympus, Tokyo, Japan), and the numbers of eosinophils counted in the lungs of each mouse were averaged as described previously (10). For immunohistochemistry, antigen retrieval of formalin-fixed mouse tissue sections was performed by autoclaving at 121°C for 10 min in retrieval solution at pH 6.0 (Nichirei, Tokyo, Japan). SARS-CoV-2 antigens were detected using a polymer-based detection system (Nichirei-Histofine simple stain mouse MAX PO, Nichirei Biosciences Inc., Tokyo, Japan), and an in-house rabbit anti-SARS-CoV-2 N antibody was used as the primary antibody. For double staining of CD3 (for T cells) and Iba-1 (for macrophages) antigens, a rabbit anti-human CD3 antibody (790-4341, Ventana Medical System, Tucson, AZ) and a rabbit anti-human Iba-1 antibody (019-19741, Wako Pure Chemical Industries, Osaka, Japan) were used. Diaminobenzidine (Sigma-Aldrich) and a Vina Green chromogen kit (Biocare Medical, CA, USA) were used as chromogens for horseradish peroxidase (HRP) visualization. Following the first staining for CD3 using the polymer-based detection system with diaminobenzidine, denaturation was performed by hydrolytic autoclaving in citrate buffer (pH 6.0) for 10 min at 121°C. The second staining was performed for Iba-1 with Vina Green. Nuclei were counterstained with hematoxylin for 10 s.

### Expression and purification of recombinant SARS-CoV-2 monomeric S protein for immunization

SARS-CoV-2 monomeric S-ect was produced using a mammalian cell protein expression system. The S gene sequence (GenBank, MN908947) was commercially synthesized (Genewiz). The extracellular region of the S sequence (amino acids 1 to 1213; MFVF...IKWP) was codon-optimized for mammalian cell expression, and the polybasic cleavage site was removed (RRAR to A) with stabilizing mutations (K986P and V987P; wild-type numbering) introduced as described by Amanat *et al.* (53). The plasmid expressing monomeric S comprised the extracellular domain of S, which was C-terminally fused to the thrombin site, and a Strep-tag II and a His tag was cloned into the PCXSN vector. S-ect was expressed using the Expi293 Expression System (Thermo Fisher Scientific), according to the manufacturer's instructions. Seven days after transfection, the medium was clarified by centrifugation at 1200g, filtered, and purified with Ni-NTA agarose (QIAGEN). The purified S-ect was concentrated using Amicon Ultracel (Merck) centrifugation units with a cutoff of 50 kDa, and the buffer was changed to PBS (pH 7.4). Proteins were filtered through a Cosmospin filter G with a pore size of 0.2 µm (Nalcalai Tesque) and stored at -80°C until use.

### Estimation of the S-specific IgG2a/IgG1 ratio

Chimeric human-mouse monoclonal antibody S309 was generated as a standard antibody for the quantification of S-specific mouse IgG1 and IgG2a antibodies. Human monoclonal antibody S309 was derived from a human memory B cell in a patient infected with SARS-CoV-2 (54). S-specific IgG1 and IgG2a levels in serum were quantified by ELISA. Trimeric S protein (ACROBiosystems, Newark,

DE) was used as a coating antigen. Serum S-specific IgG1 and IgG2a were detected by HRP-conjugated goat anti-mouse IgG1 and IgG2a antibodies, respectively, which were obtained from Bethyl Laboratories (Montgomery, TX). The enzymatic reaction was started by the addition of ABTS substrate (Roche). The absorbance at 405 nm (reference at 560 nm) was measured in an iMark microplate reader (Bio-Rad, Hercules, CA). Last, IgG2a/IgG1 ratios were calculated from the quantified values.

### Statistical analyses

All data are expressed as the mean and SEM, except for eosinophil counts (median with interquartile range) and neutralizing antibodies [geometric measure theory (GMT) + 95% confidence interval]. Statistical analyses were performed using GraphPad Prism 9 software (GraphPad Software, La Jolla, CA). Intergroup comparisons were performed using nonparametric analysis.  $P < 0.05$  was considered statistically significant. Detailed materials and methods for this study are provided in the Supplementary Materials.

### SUPPLEMENTARY MATERIALS

Supplementary material for this article is available at <https://science.org/doi/10.1126/sciadv.abh3827>

[View/request a protocol for this paper from Bio-protocol.](#)

### REFERENCES AND NOTES

- N. Zhu, D. Zhang, W. Wang, X. Li, B. Yang, J. Song, X. Zhao, B. Huang, W. Shi, R. Lu, P. Niu, F. Zhan, X. Ma, D. Wang, W. Xu, G. Wu, G. F. Gao, W. Tan; China Novel Coronavirus Investigating and Research Team, A novel coronavirus from patients with pneumonia in China, 2019. *N. Engl. J. Med.* **382**, 727–733 (2020).
- N. Chen, M. Zhou, X. Dong, J. Qu, F. Gong, Y. Han, Y. Qiu, J. Wang, Y. Liu, Y. Wei, J. Xia, T. Yu, X. Zhang, L. Zhang, Epidemiological and clinical characteristics of 99 cases of 2019 novel coronavirus pneumonia in Wuhan, China: A descriptive study. *Lancet* **395**, 507–513 (2020).
- C. Huang, Y. Wang, X. Li, L. Ren, J. Zhao, Y. Hu, L. Zhang, G. Fan, J. Xu, X. Gu, Z. Cheng, T. Yu, J. Xia, Y. Wei, W. Wu, X. Xie, W. Yin, H. Li, M. Liu, Y. Xiao, H. Gao, L. Guo, J. Xie, G. Wang, R. Jiang, Z. Gao, Q. Jin, J. Wang, B. Cao, Clinical features of patients infected with 2019 novel coronavirus in Wuhan, China. *Lancet* **395**, 497–506 (2020).
- World Health Organization, R&D blueprint and COVID-19 (2020); [www.who.int/teams/blueprint/covid-19](http://www.who.int/teams/blueprint/covid-19).
- P. H. Lambert, D. M. Ambrosino, S. R. Andersen, R. S. Baric, S. B. Black, R. T. Chen, C. L. Dekker, A. M. Didierlaurent, B. S. Graham, S. D. Martin, D. C. Molrine, S. Perlman, P. A. Picard-Fraser, A. J. Pollard, C. Qin, K. Subbarao, J. P. Cramer, Consensus summary report for CEPI/BC March 12–13, 2020 meeting: Assessment of risk of disease enhancement with COVID-19 vaccines. *Vaccine* **38**, 4783–4791 (2020).
- C. T. Tseng, E. Sbrana, N. Iwata-Yoshikawa, P. C. Newman, T. Garron, R. L. Atmar, C. J. Peters, R. B. Couch, Immunization with SARS coronavirus vaccines leads to pulmonary immunopathology on challenge with the SARS virus. *PLOS ONE* **7**, e35421 (2012).
- M. Bolles, D. Deming, K. Long, S. Agnihothram, A. Whitmore, M. Ferris, W. Funkhouser, L. Gralinski, A. Totura, M. Heise, R. S. Baric, A double-inactivated severe acute respiratory syndrome coronavirus vaccine provides incomplete protection in mice and induces increased eosinophilic proinflammatory pulmonary response upon challenge. *J. Virol.* **85**, 12201–12215 (2011).
- D. Deming, T. Sheahan, M. Heise, B. Yount, N. Davis, A. Sims, M. Suthar, J. Harkema, A. Whitmore, R. Pickles, A. West, E. Donaldson, K. Curtis, R. Johnston, R. Baric, Vaccine efficacy in senescent mice challenged with recombinant SARS-CoV bearing epidemic and zoonotic spike variants. *PLOS Med.* **3**, e525 (2006).
- F. Yasui, C. Kai, M. Kitabatake, S. Inoue, M. Yoneda, S. Yokochi, R. Kase, S. Sekiguchi, K. Morita, T. Hishima, H. Suzuki, K. Karamatsu, Y. Yasutomi, H. Shida, M. Kidokoro, K. Mizuno, K. Matsushima, M. Kohara, Prior immunization with severe acute respiratory syndrome (SARS)-associated coronavirus (SARS-CoV) nucleocapsid protein causes severe pneumonia in mice infected with SARS-CoV. *J. Immunol.* **181**, 6337–6348 (2008).
- H. Sekimukai, N. Iwata-Yoshikawa, S. Fukushi, H. Tani, M. Kataoka, T. Suzuki, H. Hasegawa, K. Niikura, K. Arai, N. Nagata, Gold nanoparticle-adjuvanted S protein induces a strong antigen-specific IgG response against severe acute respiratory syndrome-related coronavirus infection, but fails to induce protective antibodies and limit eosinophilic infiltration in lungs. *Microbiol. Immunol.* **64**, 33–51 (2020).
- N. Iwata-Yoshikawa, A. Uda, T. Suzuki, Y. Tsunetsugu-Yokota, Y. Sato, S. Morikawa, M. Tashiro, T. Sata, H. Hasegawa, N. Nagata, Effects of Toll-like receptor stimulation on eosinophil infiltration in lungs of BALB/c mice immunized with UV-inactivated severe acute respiratory syndrome-related coronavirus vaccine. *J. Virol.* **88**, 8597–8614 (2014).
- F. M. Munoz, J. P. Cramer, C. L. Dekker, M. Z. Dudley, B. S. Graham, M. Gurwith, B. Law, S. Perlman, F. P. Polack, J. M. Spergel, E. Van Braeckel, B. J. Ward, A. M. Didierlaurent, P. H. Lambert, Vaccine-associated enhanced disease: Case definition and guidelines for data collection, analysis, and presentation of immunization safety data. *Vaccine* **39**, 3053–3066 (2021).
- H. W. Kim, J. G. Canchola, C. D. Brandt, G. Pyles, R. M. Chanock, K. Jensen, R. H. Parrott, Respiratory syncytial virus disease in infants despite prior administration of antigenic inactivated vaccine. *Am. J. Epidemiol.* **89**, 422–434 (1969).
- M. R. Olson, S. M. Varga, Pulmonary immunity and immunopathology: Lessons from respiratory syncytial virus. *Expert Rev. Vaccines* **7**, 1239–1255 (2008).
- F. P. Polack, M. N. Teng, P. L. Collins, G. A. Prince, M. Exner, H. Regele, D. D. Lirman, R. Rabold, S. J. Hoffman, C. L. Karp, S. R. Kleberberger, M. Wills-Karp, R. A. Karzon, A role for immune complexes in enhanced respiratory syncytial virus disease. *J. Exp. Med.* **196**, 859–865 (2002).
- M. Connors, A. B. Kulkarni, C. Y. Firestone, K. L. Holmes, H. C. Morse III, A. V. Sotnikov, B. R. Murphy, Pulmonary histopathology induced by respiratory syncytial virus (RSV) challenge of formalin-inactivated RSV-immunized BALB/c mice is abrogated by depletion of CD4+ T cells. *J. Virol.* **66**, 7444–7451 (1992).
- M. Connors, N. A. Giese, A. B. Kulkarni, C. Y. Firestone, H. C. Morse, B. R. Murphy, Enhanced pulmonary histopathology induced by respiratory syncytial virus (RSV) challenge of formalin-inactivated RSV-immunized BALB/c mice is abrogated by depletion of interleukin-4 (IL-4) and IL-10. *J. Virol.* **68**, 5321–5325 (1994).
- M. F. Delgado, S. Covillejo, A. C. Monsalvo, G. A. Melendi, J. Z. Hernandez, J. P. Batalle, L. Diaz, A. Trento, H. Y. Chang, W. Mitzner, J. Ravetch, J. A. Melero, P. M. Irusta, F. P. Polack, Lack of antibody affinity maturation due to poor Toll-like receptor stimulation leads to enhanced respiratory syncytial virus disease. *Nat. Med.* **15**, 34–41 (2009).
- T. Sheahan, T. E. Morrison, W. Funkhouser, S. Uematsu, S. Akira, R. S. Baric, M. T. Heise, MyD88 is required for protection from lethal infection with a mouse-adapted SARS-CoV. *PLOS Pathog.* **4**, e1000240 (2008).
- Y. Honda-Okubo, D. Barnard, C. H. Ong, B. H. Peng, C. T. Tseng, N. Petrovsky, Severe acute respiratory syndrome-associated coronavirus vaccines formulated with delta inulin adjuvants provide enhanced protection while ameliorating lung eosinophilic immunopathology. *J. Virol.* **89**, 2995–3007 (2015).
- A. S. Agrawal, X. Tao, A. Algaissi, T. Garron, K. Narayanan, B. H. Peng, R. B. Couch, C. T. Tseng, Immunization with inactivated Middle East Respiratory Syndrome coronavirus vaccine leads to lung immunopathology on challenge with live virus. *Hum. Vaccin. Immunother.* **12**, 2351–2356 (2016).
- T. F. Rogers, F. Zhao, D. Huang, N. Beutler, A. Burns, W.-T. He, O. Limbo, C. Smith, G. Song, J. Woehl, L. Yang, R. K. Abbott, S. Callaghan, E. Garcia, J. Hurtado, M. Parren, L. Peng, S. Ramirez, J. Ricketts, M. J. Ricciardi, S. A. Rawlings, N. C. Wu, M. Yuan, D. M. Smith, D. Nemazee, J. R. Teijaro, J. E. Voss, I. A. Wilson, R. Andrabí, B. Briney, E. Landais, D. Sok, J. G. Jardine, D. R. Burton, Isolation of potent SARS-CoV-2 neutralizing antibodies and protection from disease in a small animal model. *Science* **369**, 956–963 (2020).
- A. Roberts, E. W. Lamirande, L. Vogel, B. Baras, G. Goossens, I. Knott, J. Chen, J. M. Ward, V. Vassilev, K. Subbarao, Immunogenicity and protective efficacy in mice and hamsters of a  $\beta$ -propiolactone inactivated whole virus SARS-CoV vaccine. *Viral Immunol.* **23**, 509–519 (2010).
- L. Bao, W. Deng, B. Huang, H. Gao, J. Liu, L. Ren, Q. Wei, P. Yu, Y. Xu, F. Qi, Y. Qu, F. Li, Q. Lv, W. Wang, J. Xue, S. Gong, M. Liu, G. Wang, S. Wang, Z. Song, L. Zhao, P. Liu, L. Zhao, F. Ye, H. Wang, W. Zhou, N. Zhu, W. Zhen, H. Yu, X. Zhang, L. Guo, L. Chen, C. Wang, Y. Wang, X. Wang, Y. Xiao, Q. Sun, H. Liu, F. Zhu, C. Ma, L. Yan, M. Yang, J. Han, W. Xu, W. Tan, X. Peng, Q. Jin, G. Wu, C. Qin, The pathogenicity of SARS-CoV-2 in hACE2 transgenic mice. *Nature* **583**, 830–833 (2020).
- K. H. Dinnon, S. R. Leist, A. Schäfer, C. E. Edwards, D. R. Martinez, S. A. Montgomery, A. West, B. L. Yount, Y. J. Hou, L. E. Adams, K. L. Gully, A. J. Brown, E. Huang, M. D. Bryant, I. C. Choong, J. S. Glenn, L. E. Gralinski, T. P. Sheahan, R. S. Baric, A mouse-adapted model of SARS-CoV-2 to test COVID-19 countermeasures. *Nature* **586**, 560–566 (2020).
- H. Gu, Q. Chen, G. Yang, L. He, H. Fan, Y.-Q. Deng, Y. Wang, Y. Teng, Z. Zhao, Y. Cui, Y. Li, X.-F. Li, J. Li, N.-N. Zhang, X. Yang, S. Chen, Y. Guo, G. Zhao, X. Wang, D.-Y. Luo, H. Wang, X. Yang, Y. Li, G. Han, Y. He, X. Zhou, S. Geng, X. Sheng, S. Jiang, S. Sun, C.-F. Qin, Y. Zhou, Adaptation of SARS-CoV-2 in BALB/c mice for testing vaccine efficacy. *Science* **369**, 1603–1607 (2020).
- N. Nagata, N. Iwata, H. Hasegawa, S. Fukushi, A. Harashima, Y. Sato, M. Saijo, F. Taguchi, S. Morikawa, T. Sata, Mouse-passaged severe acute respiratory syndrome-associated

- coronavirus leads to lethal pulmonary edema and diffuse alveolar damage in adult but not young mice. *Am. J. Pathol.* **172**, 1625–1637 (2008).
28. E. J. Williamson, A. J. Walker, K. Bhaskaran, S. Bacon, C. Bates, C. E. Morton, H. J. Curtis, A. Mehrkar, D. Evans, P. Inglesby, J. Cockburn, H. I. McDonald, B. MacKenna, L. Tomlinson, I. J. Douglas, C. T. Rentsch, R. Mathur, A. Y. S. Wong, R. Grieve, D. Harrison, H. Forbes, A. Schultze, R. Croker, J. Parry, F. Hester, S. Harper, R. Perera, S. J. W. Evans, L. Smeeth, B. Goldacre, Factors associated with COVID-19-related death using OpenSAFELY. *Nature* **584**, 430–436 (2020).
  29. A. Roberts, C. Paddock, L. Vogel, E. Butler, S. Zaki, K. Subbarao, Aged BALB/c mice as a model for increased severity of severe acute respiratory syndrome in elderly humans. *J. Virol.* **79**, 5833–5838 (2005).
  30. S. R. Leist, K. H. Dinnon III, A. Schäfer, L. V. Tse, K. Okuda, Y. J. Hou, A. West, C. E. Edwards, W. Sanders, E. J. Fritch, K. L. Gully, T. Scobey, A. J. Brown, T. P. Sheahan, N. J. Moorman, R. C. Boucher, L. E. Gralinski, S. A. Montgomery, R. S. Baric, A mouse-adapted SARS-CoV-2 induces acute lung injury and mortality in standard laboratory mice. *Cell* **183**, 1070–1085.e12 (2020).
  31. J. Wang, L. Shuai, C. Wang, R. Liu, X. He, X. Zhang, Z. Sun, D. Shan, J. Ge, X. Wang, R. Hu, G. Zhong, Z. Wen, Z. Bu, Mouse-adapted SARS-CoV-2 replicates efficiently in the upper and lower respiratory tract of BALB/c and C57BL/6J mice. *Protein Cell* **11**, 776–782 (2020).
  32. H. S. Hillen, G. Kocik, L. Farnung, C. Dienemann, D. Tegunov, P. Cramer, Structure of replicating SARS-CoV-2 polymerase. *Nature* **584**, 154–156 (2020).
  33. L. Subissi, C. C. Posthuma, A. Collet, J. C. Zevenhoven-Dobbe, A. E. Gorbalenya, E. Decroly, E. J. Snijder, B. Canard, I. Imbert, One severe acute respiratory syndrome coronavirus protein complex integrates processive RNA polymerase and exonuclease activities. *Proc. Natl. Acad. Sci. U.S.A.* **111**, E3900–E3909 (2014).
  34. S. A. Huber, B. Pfaeffle, Differential Th1 and Th2 cell responses in male and female BALB/c mice infected with coxsackievirus group B type 3. *J. Virol.* **68**, 5126–5132 (1994).
  35. N. Iwata-Yoshikawa, T. Okamura, Y. Shimizu, H. Hasegawa, M. Takeda, N. Nagata, TMPRSS2 contributes to virus spread and immunopathology in the airways of murine models after coronavirus infection. *J. Virol.* **93**, (2019).
  36. S. E. Mills, in *Histology for Pathologists* (Wolters Kluwer, ed. 5, 2020), pp. xvi, pp. 1320.
  37. K. Modjarrad, C. C. Roberts, K. T. Mills, A. R. Castellano, K. Paolino, K. Muthumani, E. L. Reuschel, M. L. Robb, T. Racine, M. D. Oh, C. Lamarre, F. I. Zaidi, J. Boyer, S. B. Kudchokar, M. Jeong, J. M. Darden, Y. K. Park, P. T. Scott, C. Remigio, A. P. Parikh, M. C. Wise, A. Patel, E. K. Duprét, K. Y. Kim, H. Choi, S. White, M. Bagarazzi, J. M. May, D. Kane, H. Lee, G. Kobinger, N. L. Michael, D. B. Weiner, S. J. Thomas, J. N. Maslow, Safety and immunogenicity of an anti-Middle East respiratory syndrome coronavirus DNA vaccine: A phase 1, open-label, single-arm, dose-escalation trial. *Lancet Infect. Dis.* **19**, 1013–1022 (2019).
  38. Z. Song, Y. Xu, L. Bao, L. Zhang, P. Yu, Y. Qu, H. Zhu, W. Zhao, Y. Han, C. Qin, From SARS to MERS, thrusting coronaviruses into the spotlight. *Viruses* **11**, 59 (2019).
  39. L. A. Jackson, E. J. Anderson, N. G. Roush, P. C. Roberts, M. Makhene, R. N. Coler, M. P. McCullough, J. D. Chappell, M. R. Denison, L. J. Stevens, A. J. Pruijssers, A. McDermott, B. Flach, N. A. Doria-Rose, K. S. Corbett, K. M. Morabito, S. O'Dell, S. D. Schmidt, P. A. Swanson II, M. Padilla, J. R. Mascola, K. M. Neuzil, H. Bennett, W. Sun, E. Peters, M. Makowski, J. Albert, K. Cross, W. Buchanan, R. Pikaart-Tautges, J. E. Ledgervood, B. S. Graham, J. H. Beigel, An mRNA vaccine against SARS-CoV-2—Preliminary report. *N. Engl. J. Med.* **383**, 1920–1931 (2020).
  40. E. E. Walsh, R. W. French Jr., A. R. Falsey, N. Kitchin, J. Absalon, A. Gurtman, S. Lockhart, K. Neuzil, M. J. Mulligan, R. Bailey, K. A. Swanson, P. Li, K. Koury, W. Kalina, D. Cooper, C. Fontes-Garfias, P. Y. Shi, Ö. Türeci, K. R. Tompkins, K. E. Lyke, V. Raabe, P. R. Dormitzer, K. U. Jansen, Ü. Şahin, W. C. Gruber, Safety and immunogenicity of two RNA-based Covid-19 vaccine candidates. *N. Engl. J. Med.* **383**, 2439–2450 (2020).
  41. J. Yu, L. H. Tostanoski, L. Peter, N. B. Mercado, K. McMahan, S. H. Mahrokhian, J. P. Nikolola, J. Liu, Z. Li, A. Chandrashekhar, D. R. Martinez, C. Loos, C. Atyeo, S. Fischinger, J. S. Burke, M. D. Stein, Y. Chen, A. Zuiani, F. J. N. Lelis, M. Travers, S. Habibi, L. Pessant, A. Van Ry, K. Blade, R. Brown, A. Cook, B. Finneyfrock, A. Dodson, E. Teow, J. Velasco, R. Zahn, F. Wegmann, E. A. Bondzie, G. Dagotto, M. S. Gebre, X. He, C. Jacob-Dolan, M. Kirilova, N. Kordana, Z. Lin, L. F. Maxfield, F. Nampanya, R. Nityanandam, J. D. Ventura, H. Wan, Y. Cai, B. Chen, A. G. Schmidt, D. R. Wesemann, R. S. Baric, G. Alter, H. Andersen, M. G. Lewis, D. H. Barouch, DNA vaccine protection against SARS-CoV-2 in rhesus macaques. *Science* **369**, 806–811 (2020).
  42. S. Plotkin, History of vaccination. *Proc. Natl. Acad. Sci. U.S.A.* **111**, 12283–12287 (2014).
  43. Y. Dong, T. Dai, Y. Wei, L. Zhang, M. Zheng, F. Zhou, A systematic review of SARS-CoV-2 vaccine candidates. *Signal Transduct. Target. Ther.* **5**, 237 (2020).
  44. T. Sheahan, A. Whitmore, K. Long, M. Ferris, B. Rockx, W. Funkhouser, E. Donaldson, L. Gralinski, M. Collier, M. Heise, N. Davis, R. Johnston, R. S. Baric, Successful vaccination strategies that protect aged mice from lethal challenge from influenza virus and heterologous severe acute respiratory syndrome coronavirus. *J. Virol.* **85**, 217–230 (2011).
  45. R. L. Tillett, J. R. Sevinsky, P. D. Hartley, H. Kerwin, N. Crawford, A. Gorzalski, C. Laverdure, S. C. Verma, C. C. Rossetto, D. Jackson, M. J. Farrell, S. Van Hooser, M. Pandori, Genomic evidence for reinfection with SARS-CoV-2: A case study. *Lancet Infect. Dis.* **21**, 52–58 (2021).
  46. R. Sharma, S. Sardar, A. Mohammad Arshad, F. Ata, S. Zara, W. Munir, A patient with asymptomatic SARS-CoV-2 infection who presented 86 days later with COVID-19 pneumonia possibly due to reinfection with SARS-CoV-2. *Am. J. Case Rep.* **21**, e927154 (2020).
  47. S. Matsuyama, N. Nao, K. Shirato, M. Kawase, S. Saito, I. Takayama, N. Nagata, T. Sekizuka, H. Katoh, F. Kato, M. Sakata, M. Tahara, S. Kutsuna, N. Ohmagari, M. Kuroda, T. Suzuki, T. Kageyama, M. Takeda, Enhanced isolation of SARS-CoV-2 by TMPRSS2-expressing cells. *Proc. Natl. Acad. Sci. U.S.A.* **117**, 7001–7003 (2020).
  48. K. Shirato, N. Nao, H. Katano, I. Takayama, S. Saito, F. Kato, H. Katoh, M. Sakata, Y. Nakatsu, Y. Mori, T. Kageyama, S. Matsuyama, M. Takeda, Development of genetic diagnostic methods for detection for novel coronavirus 2019(nCoV-2019) in Japan. *Jpn. J. Infect. Dis.* **73**, 304–307 (2020).
  49. H. Li, R. Durbin, Fast and accurate short read alignment with Burrows-Wheeler transform. *Bioinformatics* **25**, 1754–1760 (2009).
  50. A. Souvorov, R. Agarwalla, D. J. Lipman, SKESA: Strategic k-mer extension for scrupulous assemblies. *Genome Biol.* **19**, 153 (2018).
  51. D. Coil, G. Jospin, A. E. Darling, A5-miseq: An updated pipeline to assemble microbial genomes from Illumina MiSeq data. *Bioinformatics* **31**, 587–589 (2015).
  52. D. C. Koboldt, Q. Zhang, D. E. Larson, D. Shen, M. D. McLellan, L. Lin, C. A. Miller, E. R. Mardis, L. Ding, R. K. Wilson, VarScan 2: Somatic mutation and copy number alteration discovery in cancer by exome sequencing. *Genome Res.* **22**, 568–576 (2012).
  53. F. Amanat, D. Stadlbauer, S. Strohmeier, T. H. O. Nguyen, V. Chromikova, M. McMahon, K. Jiang, G. A. Arunkumar, D. Jurczyszak, J. Polanco, M. Bermudez-Gonzalez, G. Kleiner, T. Aydillo, L. Miorin, D. S. Fierer, L. A. Lugo, E. M. Kojic, J. Stoever, S. T. H. Liu, C. Cunningham-Rundles, P. L. Felgner, T. Moran, A. García-Sastre, D. Caplivski, A. C. Cheng, K. Kedzierska, O. Vapalahti, J. M. Hepojoki, V. Simon, F. Krammer, A serological assay to detect SARS-CoV-2 seroconversion in humans. *Nat. Med.* **26**, 1033–1036 (2020).
  54. D. Pinto, Y. J. Park, M. Beltramello, A. C. Walls, M. A. Tortorici, S. Bianchi, S. Jaconi, K. Culap, F. Zatta, A. De Marco, A. Peter, B. Guarino, R. Spreafico, E. Cameroni, J. B. Case, R. E. Chen, C. Havenar-Daughton, G. Snell, A. Teleni, H. W. Virgin, A. Lanzavecchia, M. S. Diamond, K. Fink, D. Veesler, D. Corti, Cross-neutralization of SARS-CoV-2 by a human monoclonal SARS-CoV antibody. *Nature* **583**, 290–295 (2020).

**Acknowledgments:** We thank S. Matsuyama and M. Takeda (National Institute of Infectious Disease) for providing SARS-CoV-2 isolates. We are grateful to M. Ozaki and T. Yoshida for technical assistance and our colleagues at the Institute for helpful discussions. We thank the members of the Management Department of Biosafety and Laboratory Animals for support with the BSL3 facility. **Funding:** N.I.-Y. was supported by the Grant-in-Aid for Scientific Research from the Ministry of Education, Culture, Sports, Science, and Technology in Japan (19K08945). N.N. was supported by the Grant-in-Aid for Scientific Research from the Ministry of Education, Culture, Sports, Science, and Technology in Japan (18H02665) and Japan Agency for Medical Research and Development grant (JP19fk0108072). M.Ku. was supported by Japan Agency for Medical Research and Development grant (JP20fk0108103). H.H. was supported by Japan Agency for Medical Research and Development grant (JP19fk0108112). T.Su. was supported by Japan Agency for Medical Research and Development grants (JP19fk0108104, JP19fk0108110, JP20fk0108104, JP20wm0125008, JP21fk0108104, and JP21wm0125008). **Author contributions:** Conceptualization: N.I.-Y., H.H., T.Su., and N.N. Methodology: N.I.-Y., N.S., T.Se., K.S., A.A., M.Ka., M.Ku., and N.N. Investigation: N.I.-Y., N.S., T.Se., K.S., A.A., T.H., and N.N. Visualization: N.I.-Y., N.S., T.Se., A.A., and N.N. Funding acquisition: N.I.-Y., M.K., H.H., T.S., and N.N. Project administration: M.K., H.H., and T.S. Supervision: M.K., H.H., and T.S. Writing—Original draft: N.I.-Y., N.S., T.Se., K.S., A.A., and N.N. Writing—Review and editing: N.I.-Y., N.S., T.Se., K.S., A.A., T.H., M.Ka., M.Ku., H.H., T.Su., and N.N. **Competing interests:** The authors declare that they have no competing interest. **Data and materials availability:**

The full-genome sequence of strain QHmusX was deposited in the DNA Data Bank of Japan ([www.ddbj.nig.ac.jp/index.html](http://www.ddbj.nig.ac.jp/index.html)) under accession no. LC605054. All short-read sequences were deposited in the DNA Data Bank of Japan (BioProject PRJDB11095, DRA accession no. DRA011496). All raw RNA sequencing FASTQ files were uploaded to the DNA Data Bank of Japan Sequence Read Archive (BioProject accession no. PRJDB11095 and accession no. DRA011497). All data needed to evaluate the conclusions in the paper are present in the paper and/or the Supplementary Materials. All unique/stable reagents generated in this study are available from the corresponding author upon furnishing a completed material transfer agreement. The mouse-passaged isolate (QHmusX) from SARS-CoV-2 can be provided by National Institute of Infectious Diseases pending scientific review and a completed material transfer agreement. Requests for the QHmusX should be submitted to the corresponding author, N.N.

Submitted 4 March 2021

Accepted 12 November 2021

Published 7 January 2022

10.1126/sciadv.abb3827